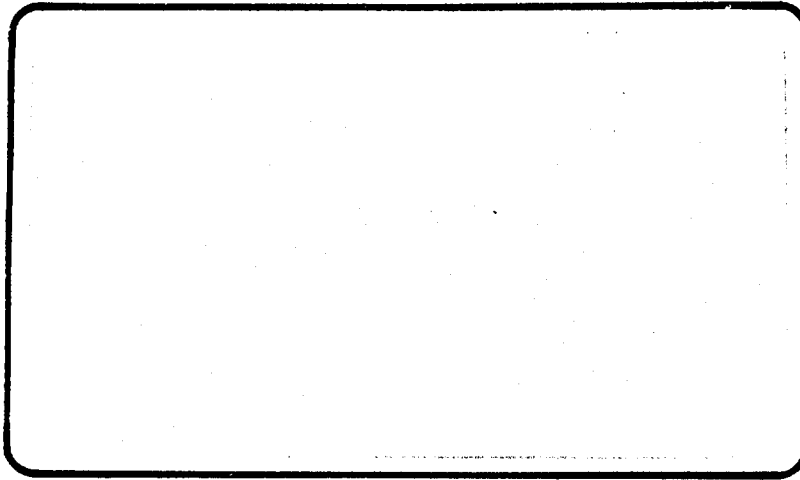
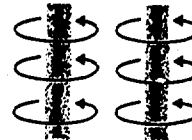


12



AD A118294

# GT - Devices



**DTIC**  
**ELECTE**  
AUG 17 1982  
**S** **D**  
**F**

DTIC FILE COPY

**DISTRIBUTION STATEMENT A**  
Approved for public release;  
Distribution Unlimited

5705A General Washington Drive

Alexandria, VA 22312

(703) 642-8150

82 08 17 003

PROJECTILE ABLATION AND  
SURVIVAL IN MASS ACCELERATORS  
USING HIGH ENERGY DENSITY PLASMAS  
FOR MASS ACCELERATION

GT-DEVICES

June 1982

Final Report

Submitted to:

Army Research Office  
P. O. Box 12211  
(Attn: Dr. F.Schmiedeshoff)  
Research Triangle Park  
North Carolina 27709

Contract No. DAAG29-81-C-0011  
ARO Project #1L161102BH57-06

Principal Investigators: D. A. Tidman and S. A. Goldstein  
One-Dimensional Hydrodynamic Model: R. F. Hubbard  
Detailed Physics Model: N. K. Winsor

Period Covered: 22 June 1981 - 21 June 1982

UNCLASSIFIED

SECURITY CLASSIFICATION OF THIS PAGE (When Data Entered)

REPORT DOCUMENTATION PAGE		READ INSTRUCTIONS BEFORE COMPLETING FORM
1. REPORT NUMBER 17917.1-EG-S	2. GOVT ACCESSION NO. A118294	3. RECIPIENT'S CATALOG NUMBER
4. TITLE (and Subtitle) Projectile Ablation and Survival in Mass Accelerators Using High Energy Density Plasmas for Mass Acceleration		5. TYPE OF REPORT & PERIOD COVERED Final: 22 Jun 81 - 21 Jun 82
7. AUTHOR(s) D. A. Tidman S. A. Goldstein		6. PERFORMING ORG. REPORT NUMBER
9. PERFORMING ORGANIZATION NAME AND ADDRESS GT-Devices Alexandria, VA 22312		8. CONTRACT OR GRANT NUMBER(s) DAAG29 81 C 0011
11. CONTROLLING OFFICE NAME AND ADDRESS U. S. Army Research Office Post Office Box 12211 Research Triangle Park, NC 27709		10. PROGRAM ELEMENT, PROJECT, TASK AREA & WORK UNIT NUMBERS
14. MONITORING AGENCY NAME & ADDRESS (if different from Controlling Office)		12. REPORT DATE Jun 82
		13. NUMBER OF PAGES 46
		15. SECURITY CLASS. (of this report) Unclassified
		15a. DECLASSIFICATION/DOWNGRADING SCHEDULE
16. DISTRIBUTION STATEMENT (of this Report)  Approved for public release; distribution unlimited.		
17. DISTRIBUTION STATEMENT (of the abstract entered in Block 20, if different from Report)  NA		
18. SUPPLEMENTARY NOTES The view, opinions, and/or findings contained in this report are those of the author(s) and should not be construed as an official Department of the Army position, policy, or decision, unless so designated by other documentation.		
19. KEY WORDS (Continue on reverse side if necessary and identify by block number) ablation projectiles mass accelerators		
20. ABSTRACT (Continue on reverse side if necessary and identify by block number) Two theoretical methods have been developed for analyzing ablation in MAID projectile accelerators. A one-dimensional model determines the effect of shocks on the ablating layer. It resolves the boundary layer of the plasma-solid interface, and demonstrates shock formation in the plasma. A detailed physics model incorporates detailed chemistry and determines the global average properties of an experimental mass accelerator. Results of experiments are compared with simulations. Excellent agreement is found. Two-dimensional ablation effects are illustrated.		

DD FORM 1 JAN 73 1473

EDITION OF 1 NOV 65 IS OBSOLETE

UNCLASSIFIED

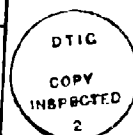
82 08 17 008

SECURITY CLASSIFICATION OF THIS PAGE (When Data Entered)

## CONTENTS

	<u>Page</u>
I. ABSTRACT. . . . .	1
II. INTRODUCTION. . . . .	2
III. ONE-DIMENSIONAL HYDRODYNAMICS MODEL . . . . .	4
A. Model Description . . . . .	4
B. Basic Results . . . . .	8
C. Nonideal Effects. . . . .	14
IV. DETAILED PHYSICS MODEL. . . . .	26
A. Equation of State . . . . .	33
B. Radiation . . . . .	34
C. Comparison with Experiment. . . . .	36
V. SUMMARY . . . . .	43

Accession For	
FTIS CRA&I	<input checked="" type="checkbox"/>
DTIC TAB	<input checked="" type="checkbox"/>
Unannounced	<input type="checkbox"/>
Justification	<input type="checkbox"/>
By	
Distribution/	
Availability Codes	
Dist	Avail and/or Special



## ABSTRACT

Two theoretical methods have been developed for analyzing ablation in MAID projectile accelerators. A one-dimensional model determines the effect of shocks on the ablating layer. It resolves the boundary layer of the plasma-solid interface, and demonstrates shock formation in the plasma. A detailed physics model incorporates detailed chemistry and determines the global average properties of an experimental mass accelerator. Results of experiments are compared with simulations. Excellent agreement is found. Two-dimensional ablation effects are illustrated.

## II. INTRODUCTION

Using high pressure plasma jets, projectiles have been propelled to velocities an order of magnitude higher than those of conventional guns. These plasma jets ablate material off the projectile and the walls of the accelerating device. The details of this ablation process significantly affect the projectile dynamics.

The nature of the ablation depends on the method of plasma production. The plasmas being used for this purpose in our laboratory are principally produced in z-pinch discharges that are either wall confined (for small radius discharges) or imploded and magnetic field confined (for initially large radius discharges). In all of these schemes plasma is directed on to the back surface of a projectile as shown in Figure 1 to generate extremely high propulsion pressures.

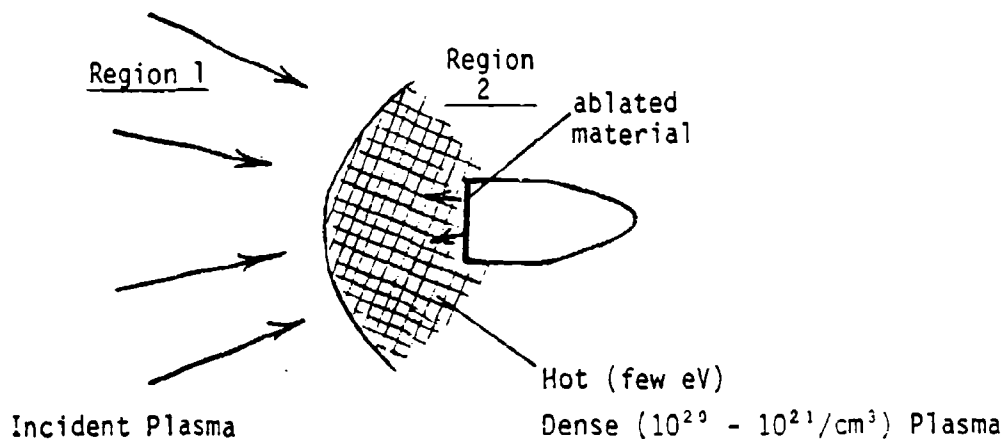


Figure 1

Projectile Acceleration by High Pressure Plasma Jets

In this theoretical program, the objective is the analysis and computer modeling of the ablation phenomena that occur when high temperature (few eV) dense ( $10^{20}$ - $10^{21}$ /cm<sup>3</sup>) plasmas are in contact with the projectile and various plasma-confining walls of the mass accelerator. These ablation phenomena play a central role in determining the lifetime of such mass accelerator components (for various materials choices) and thus its potential for repetitive firing.

For a projectile subjected to a repetitive or extended acceleration, this ablation process may affect the stability of the acceleration. Depending upon the choice of projectile materials, the maximum velocity may also be limited, because of projectile mass loss.

Two codes have been developed to analyze essential parts of these ablation processes. They are:

(i) A hydro-code in which the plasma layer (region 2 in Fig. 1) is treated as a 1D laminar flow region including energy deposition, thermal conduction, radiation diffusion and non-ideal material properties of the projectile surface layer. This model treats shock propagation and plasma motion in detail while simplifying other aspects of ablation physics.

(ii) The detailed physics code includes plasma chemistry, radiation and energy deposition models, and other features necessary to simulate actual experiments. It determines the density, temperature, and velocity of plasma incident on the projectile. This information is derived from a model for the intense z-discharge plasma source. Black body radiation is assumed to be emitted from region 2 (Fig. 1) onto the projectile

surface and the ablated material resulting from this radiation flux is calculated.

Sections III and IV of this report present more detailed descriptions of these two codes, together with some results for parameters typical of the accelerator experiments currently in progress. Section V summarizes the key results of this report.

### III. ONE-DIMENSIONAL HYDRODYNAMICS MODEL

#### a. Model Description

The ablation hydrodynamics model is a fluid-particle hybrid computer code which is able to treat a wide range of problems associated with the MAID system. It is currently being used to study the interaction between the solid surface of the projectile and the hot jet of plasma produced by the discharge. In this section, we describe the ablation hydro model equations and the numerical techniques used to solve them. In Section (III.b), we present some preliminary results from the model which emphasize the role of convection and shock propagation. Quantitative results using a more detailed treatment of radiation transport, thermal conduction, and an improved equation of state are presented in Section III.c. These processes are already included in an approximate way in the physics code model described in Section IV.

The model uses the grid and particle ("GAP") method developed by Marder to treat the convective terms in the hydrodynamic equations. The one-dimensional equations are:



$$\frac{\partial \rho}{\partial t} + \frac{\partial}{\partial x} (\rho V) = 0 \quad (1)$$

$$\frac{\partial V}{\partial t} + V \frac{\partial V}{\partial x} + \frac{1}{\rho} \frac{\partial p}{\partial x} = 0 \quad (2)$$

$$\frac{\partial}{\partial t} \left( \frac{3}{2} p + \epsilon \right) + \frac{\partial}{\partial x} \left( \frac{3}{2} p V + V \epsilon \right) + p \frac{dV}{dx} \quad (3)$$

$$= P_{\text{dep}} + \frac{\partial}{\partial x} \left( K \frac{\partial T}{\partial x} \right) - L .$$

Here  $t$  and  $x$  are the time and spatial variables,  $\rho$  is the mass density,  $V$  is the local fluid velocity,  $\epsilon$  is the thermal energy, and  $T$  is the temperature. The right side of the energy equation (3) can include power deposition from ohmic heating ( $P_{\text{dep}}$ ), radiation diffusion and thermal conduction (which are contained in the diffusion coefficient  $K$ ), and  $L$ , losses such as evaporation energy. In addition, we close the system with an equation of state:

$$(z+1)T \left( \frac{\gamma-1}{n} \right) \epsilon , \quad (4)$$

where  $\gamma$  is the usual thermodynamic ratio of specific heats and is 5/3 for an ideal gas. The number density  $n = \rho/m$  where  $m$  is the mass of an individual molecule.

The GAP method follows the motion of a large ( $\sim 2500$ ) number of fluid "particles" moving on a fixed grid. Each "particle" carries with it a position  $X$ , velocity  $V$ , specific energy  $E$ , and specific volume  $U$ . The force on each particle is evaluated by calculating  $\frac{dp}{dx}$  on the grid, and the resulting force is used to advance the positions and velocities. Next, the specific volume and energy for each particle are calculated using the thermodynamic relation  $dE = pdU$ . After

accumulating the various particle quantities onto the fluid grid, the resulting fluid quantities are projected back onto the individual particles using a linear interpolation scheme. The process is repeated at each time step. Except for the pressure gradient, the need to take spatial derivatives is eliminated. This makes it possible for the code to treat shocks without resorting to a fine spatial mesh.

The right hand side of Eq. (3) is treated using a "time-split" technique. At each time step, Eq. (3) is solved using the "GAP" method with the right hand side set equal to zero. The right hand side is treated by solving

$$\frac{\partial T}{\partial t} = \left( \frac{n}{\gamma-1} \right) \left[ p_{\text{dep}} + \frac{\partial}{\partial x} \left( K \frac{\partial T}{\partial x} \right) - L \right] \quad (5)$$

This is a diffusion equation which can be solved using standard implicit numerical techniques. The updated value of  $T$  is then incorporated into  $\epsilon$  using Eq. (4).

The diffusion coefficient  $K = K_{\text{rad}} + K_T$ , incorporating both radiation diffusion and thermal conduction. We normally assume that the solid and plasma are  $\text{CH}_2$  (polyethylene) and its dissociated constituents:  $\text{CH}$ ,  $\text{C}$ ,  $\text{H}$  and electrons, with a carbon charge state  $Z$ . The resulting thermal conduction coefficient is (in c.g.s. units)

$$K_T = \frac{2.8 \times 10^9 T_{\text{ev}}^{5/2}}{2\pi\Lambda} \left( \frac{2+Z}{2+Z^2} \right) \quad (6)$$

The coulomb logarithm ( $2\pi\Lambda$ ) is assumed to be constant.

Radiation diffusion is described by the Rosseland opacity

$$K_R = \frac{16}{3} \sigma_{\text{SB}} T^3 \lambda_{\text{abs}} \quad (7)$$

Here  $\sigma_{SB}$  is the Stefan-Boltzmann constant, and the radiation absorption length  $\lambda_{abs}$  is [for  $C + 2H + (2 + Z)e$ ]:

$$\lambda_{abs} = \frac{0.2 T_{eV}^{7/2}}{(2 + Z^2)(2 + Z)} \left( \frac{10^{19}}{n_c} \right)^2. \quad (8)$$

Note that the carbon number density is  $n_c = \rho/14 m_p$ , where  $m_p$  is the proton mass.

The ablation hydro code can be initialized in several ways. In the simplest option, the model is divided into a "solid" region ( $x < x_s$ ) and a "plasma" region ( $x > x_s$ ). In the solid region,  $n_c = 4 \times 10^{22} \text{ cm}^{-3}$ ,  $T(x) = 0.3 \text{ eV}$ , and  $V(x) = 0$  at  $t = 0$ . In the plasma region at  $t = 0$ ,  $n_c(x) \approx n_{p0} \sim 10^{20} - 10^{21} \text{ cm}^{-3}$ ,  $T_e(x)$  is a few eV, and  $v(x)$  can be either zero or any specified value consistent with the sound speed. A transition region of typically 5 grid cells bridges the two regions. In more recent versions, a specified ohmic deposition rate  $P_{dep}(x, t)$  is used. This rate is chosen so that  $T_e(x > x_s)$  approaches the desired value of a few eV for long times. In the detailed physics model described in Section III, ohmic deposition is treated self-consistently by coupling the plasma resistivity to the rest of the system circuit.

Much of the physics of the ablation process is dependent on the equation of state (Eq. (4)). In the detailed physics model, the full SESAME equation of state tables are used. In order to save computer time, we have attempted to use analytical fits to the SESAME table in the hydro code. The factor  $\gamma$  in Eq. (4) in the  $10^{20} - 10^{21} \text{ cm}^{-3}$  is well represented by

$$\gamma - 1 = C_0 e^{-\tilde{\epsilon}/\epsilon^*}, \quad (9)$$

where  $C_0 = 0.5$ ,  $\epsilon^* = 2.3$  eV and  $\tilde{\epsilon}$  is the energy per particle in eV. Unfortunately, this simple expression becomes inaccurate in the high density, low temperature region near and within the solid, where it predicts that  $\gamma - 1 \approx 0$ . Modifications to Eq. (6) which deal with this problem are discussed in the following section. The best future course appears to be to develop an efficient table look-up algorithm so that the SESAME tables can be incorporated into the hydro code.

#### b. Basic Results

The earliest version of our model treated a cold plasma jet of uniform density striking a much higher density target. This was a variation of the problem treated by Barry Marder in the original GAP code. After 100 time steps, the code revealed the formation of a density plateau in reasonable agreement with theoretical predictions. The local fluid velocity showed the expected stagnation in the region behind the reflected shock. Finally, plots of the pressure  $p(x)$  showed the expected rise in the reflected shock region as well as shock propagation in the target region.

The following figures show results from a more recent version of the model. A finite temperature has been added to both the solid and plasma, and the initial plasma density has a spatial profile as shown in Fig. 2. The local temperature is now calculated using Eq. (4), and a constant diffusion coefficient  $K$  has been added to show the effects of diffusion in the energy equation (3). The plasma initially moves to the left with a velocity  $V_0$  corresponding to the thermal velocity

# DENSITY PROFILES AT 3 TIMES (STANDARD CASE)

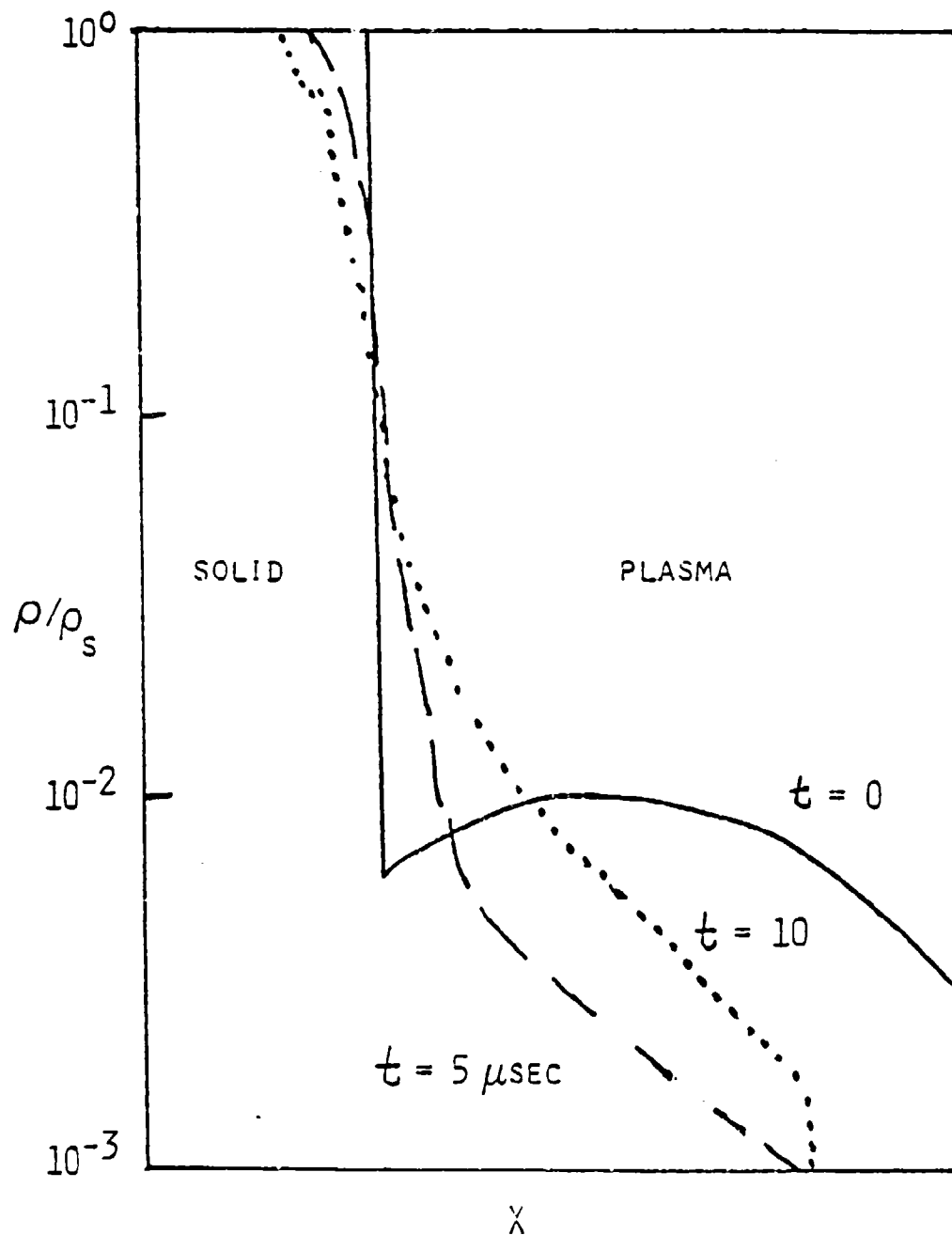


Figure 2

Plasma is initially moving to the left. It is later reflected and causes compression and ablation of solid.

for a 2.5 eV plasma temperature. Since the temperature and density dependence of  $K$  has been omitted, dimensionless units can still be used. However, for convenience we express  $t$  in microseconds.

Figure 2 shows the spatial evolution of the density profile. The slug of plasma strikes the solid and is reflected, and the density in the transition region contains a mixture of reflected plasma and ablated material. The compression of the solid and loss of material can also be observed.

Figure 3 shows the local flow velocity for the same case. Initially  $V = 0$  in the solid and  $-V_{th}$  in the gas. At  $t = 5 \mu\text{sec}$ , most of the plasma is still moving to the left except for a stagnation region close to the target. At  $t = 10 \mu\text{sec}$ , the bulk of the plasma has been reflected from the solid and has  $V > 0$ .

Figure 4 shows the corresponding temperature profiles. If the solid is initially at room temperature,  $T_{go} \approx 2.5 \text{ eV}$ . At  $t = 5 \mu\text{sec}$ , shock heating close to the solid-plasma boundary leads to a sharp temperature peak. This peak, which moves to the right, is perhaps the best indicator of the reflected shock propagating through the plasma. The figure also reveals the temperature rise in the solid. Note that most of the solid-plasma interface region lies well below the evaporation energy of  $\sim 1 \text{ eV}$ . This is likely to lead to an overestimate of the ablation rate by allowing material to be removed without the necessary investment in internal energy. A more careful treatment of this process is included in later versions of the code which contain a more realistic equation of state.

# LOCAL FLOW VELOCITY FOR STANDARD CASE

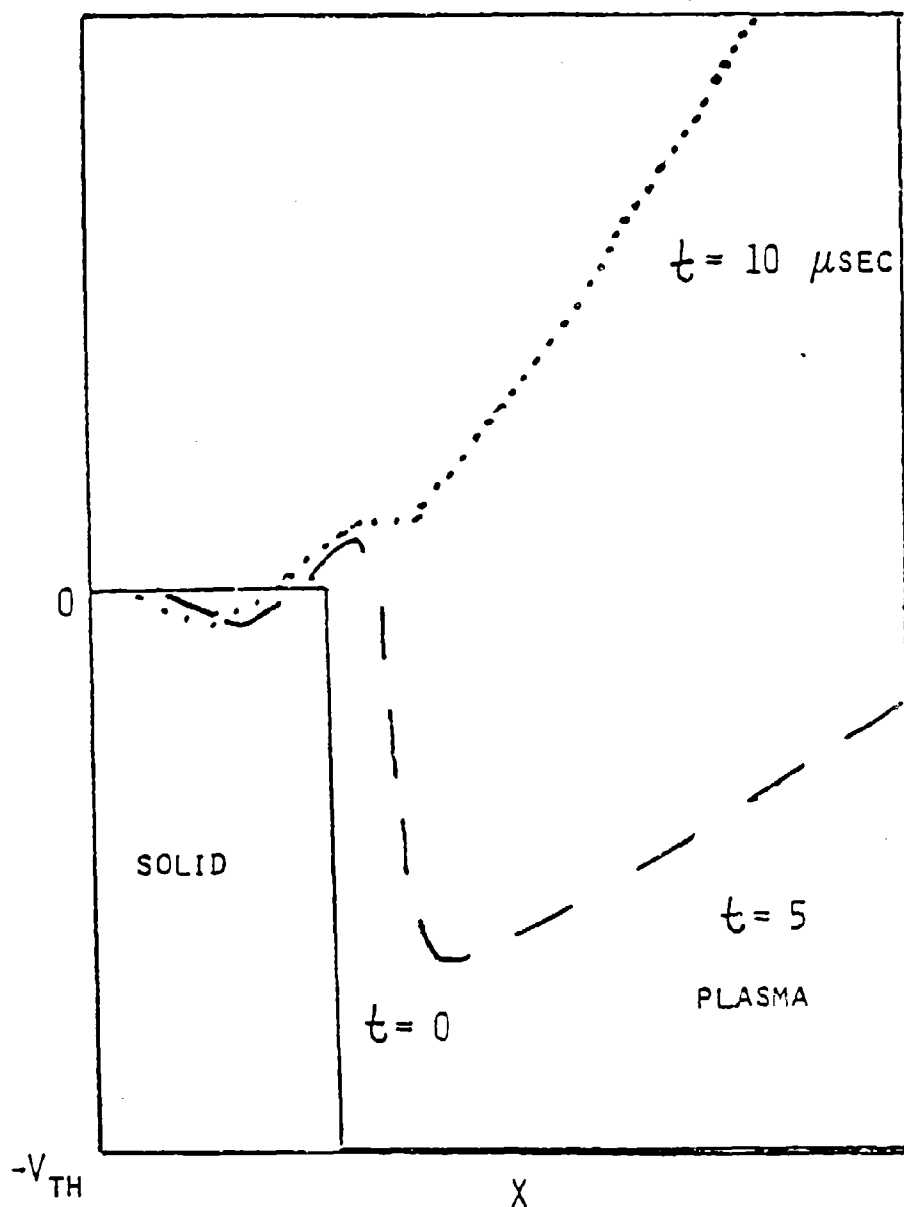


Figure 3

Initial flow velocity is zero in solid and  $\sim 5$  km/sec in plasma.  
Reflected plasma results in  $V > 0$  after  $10 \mu\text{sec}$ .

# TEMPERATURE PROFILES FOR STANDARD CASE

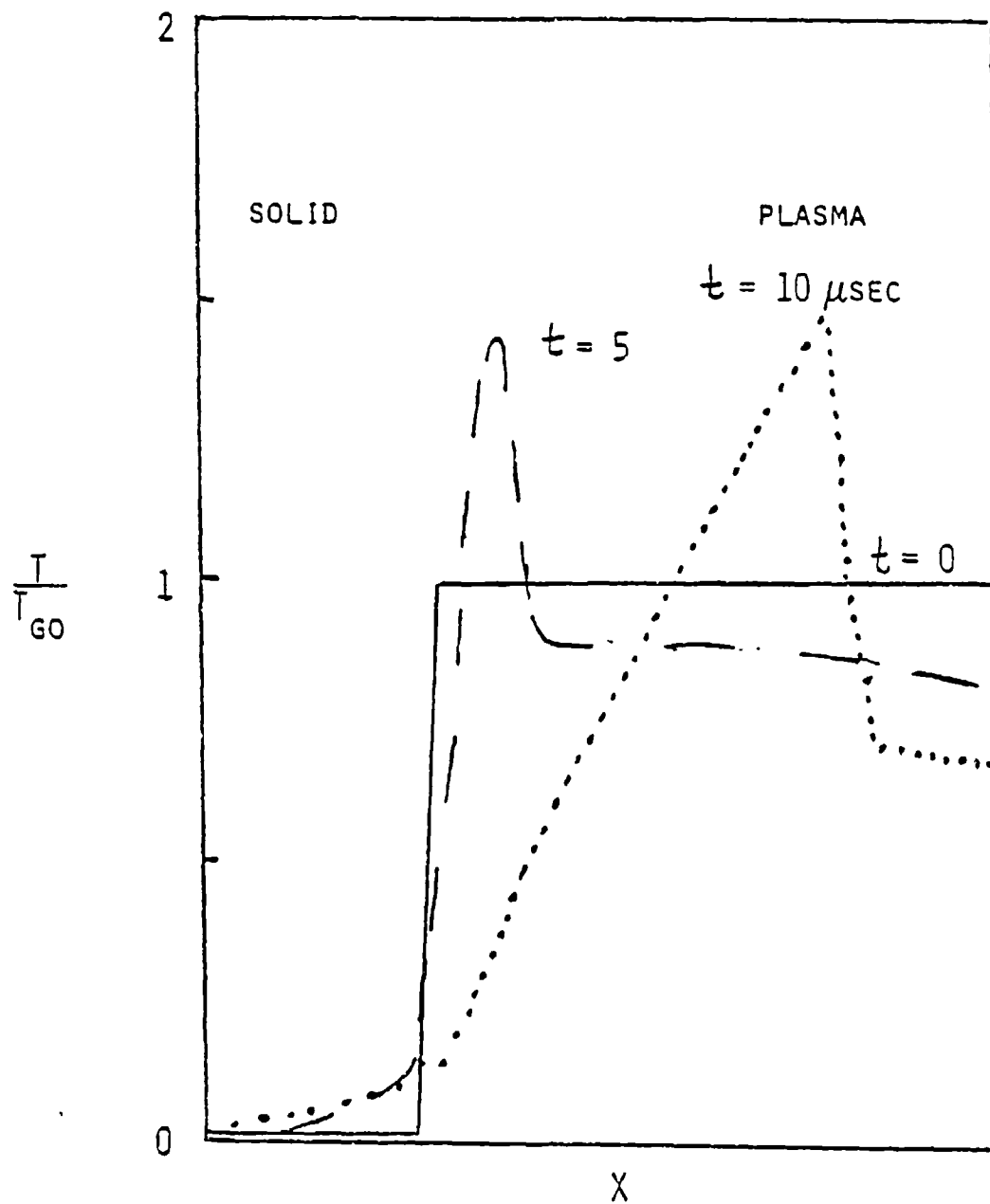


Figure 4

Temperature rise in plasma is due to shock heating. Note gradual temperature rise in solid. Most of solid-plasma interface lies below  $T_{\text{evap}} \approx 1 \text{ eV}$ .



# PRESSURE PROFILES FOR STANDARD CASE

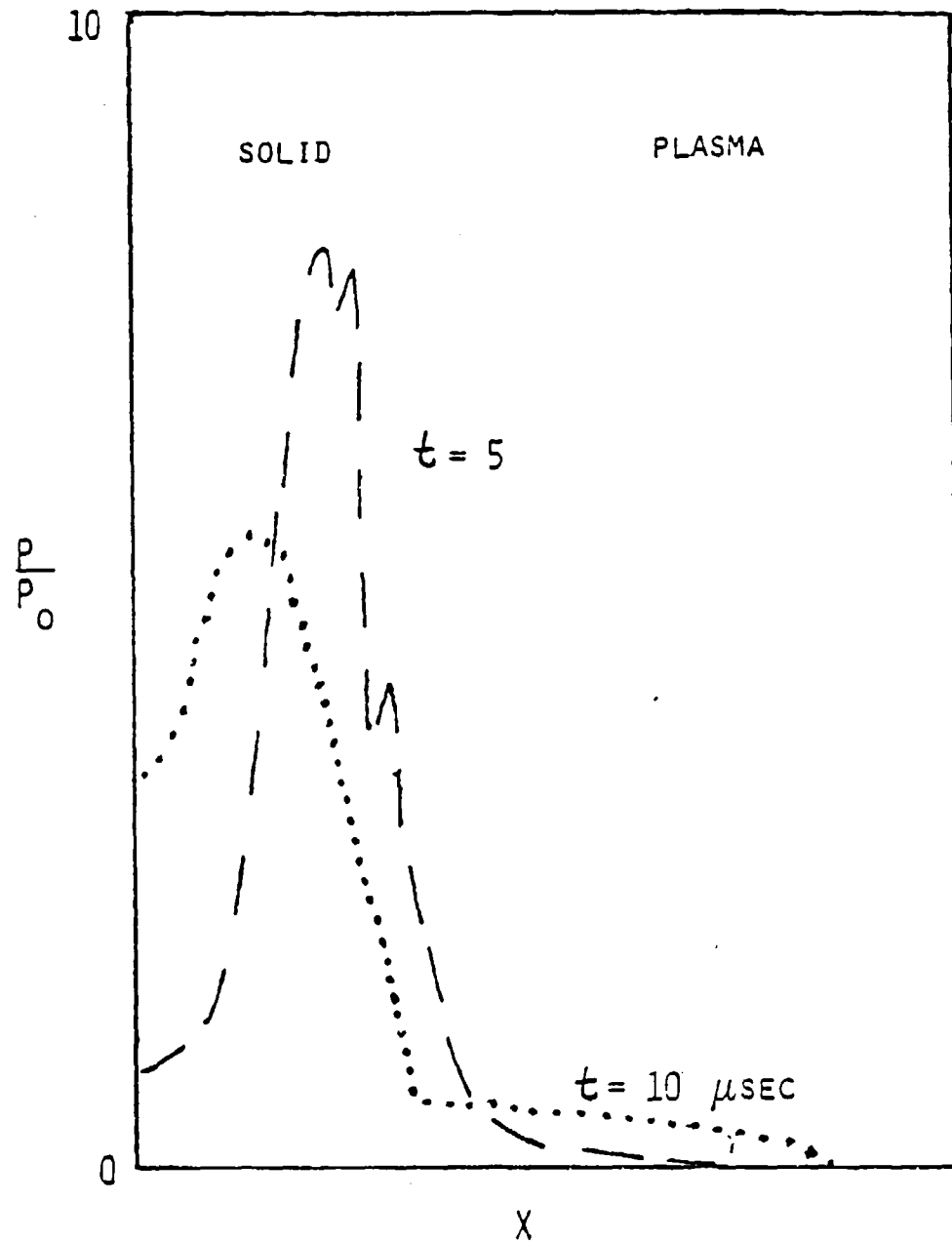


Figure 5

Pressure builds up near solid-plasma interface. Shocks propagate into the solid and are reflected back into plasma.

Finally, Figure 5 illustrates the evolution of the pressure,  $p(x)$ . There is a rapid buildup of pressure near the solid-plasma interface, and shocks propagate into the solid. Since periodic boundary conditions are used, shocks eventually reflect from the left-hand boundary back into the plasma. A more careful treatment of the solid region reduces this effect considerably, as described in the next section.

### c. Nonideal Effects

In this section, we describe more recent results with the hydro code, illustrating the effects of radiation diffusion, thermal conduction, local energy deposition, and  $\gamma$  variation in the equation-of-state. These effects can alter the evolution of the ablation process considerably. Henceforth c.g.s. units are used except where energies or temperatures in eV are shown.

Figures 6-9 describe the early stages of the ablation process for a 1 eV plasma with density  $n_{p0} = 10^{20} \text{ cm}^{-3}$  impacting a solid with a plasma flow velocity  $V_0 = 3 \times 10^5 \text{ cm/sec}$ . Equations (6) and (7) are used for  $K_T$  and  $K_R$ , and  $\gamma$  is assumed constant. The plasma number density  $n(x)$  shows the compression of the solid and the effects of material flow out from the solid (Fig. 6). The compression effect is enhanced by the presence of the nearby reflecting boundary and by the assumption of constant  $\gamma$  and thus is probably overestimated. The pressure profile (Fig. 7) shows both shock propagation into the solid as well as the reflected shock propagating away from the solid and is similar to Fig. 5 of the previous section. Both the local fluid velocity (Fig. 8) and temperature (Fig. 9) show features qualitatively similar to those seen in the dimensionless example (Figs. 3 and 4). In

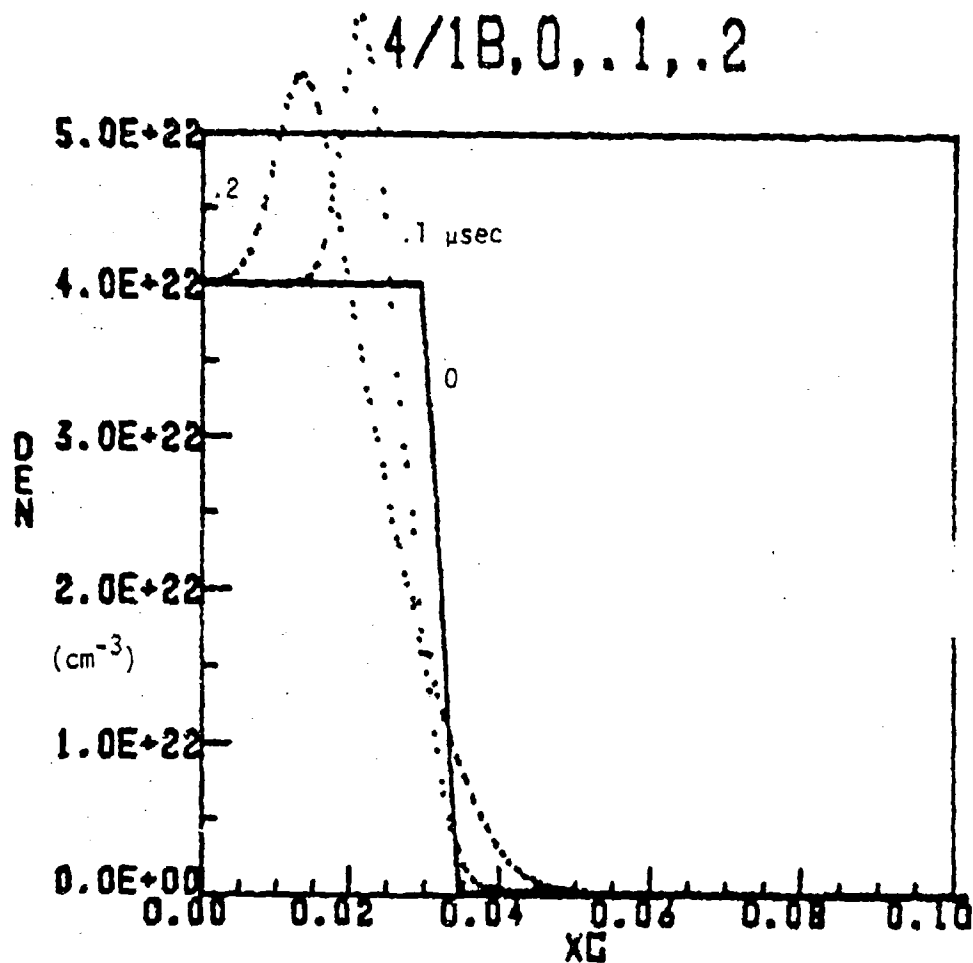


Figure 6

Carbon density  $n(x)$  at 0, 0.1, and 0.2  $\mu\text{sec}$  for a 1 eV,  $10^{20} \text{ cm}^{-3}$  plasma striking the solid at 3 km/sec.

4/1B, 0,.1,.2

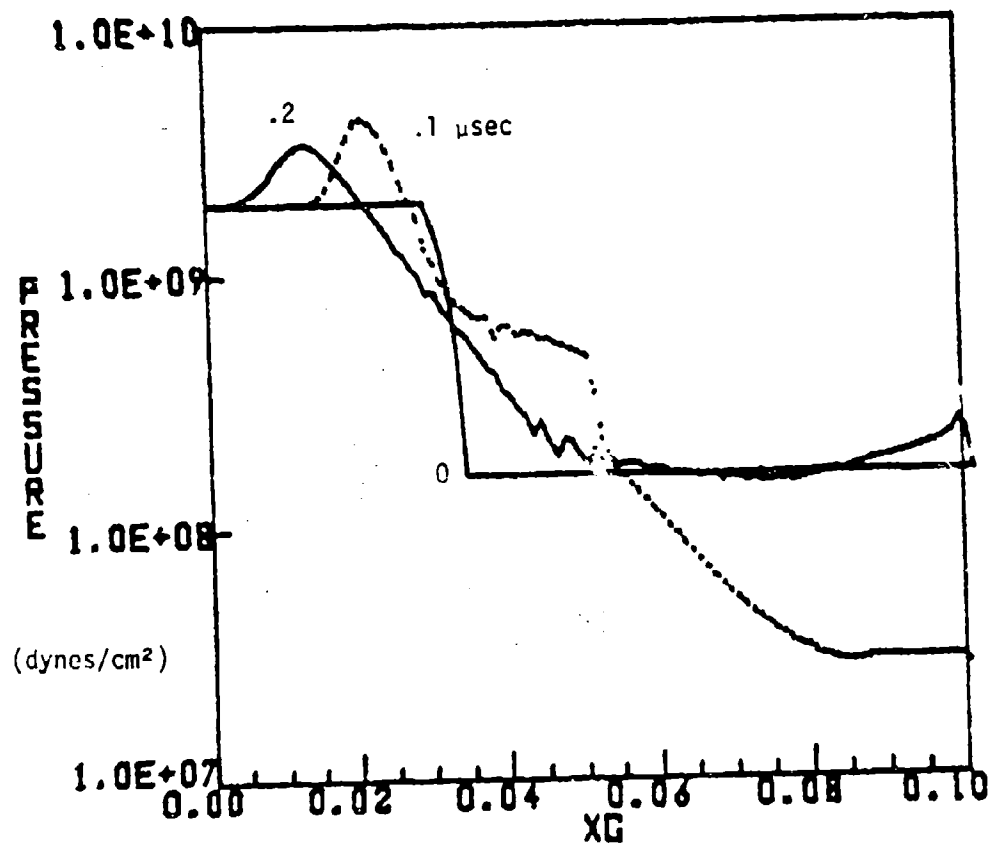


Figure 7

Pressure  $p(x)$  for the example described in Figure 6.

4/1B, 0,.1,.2

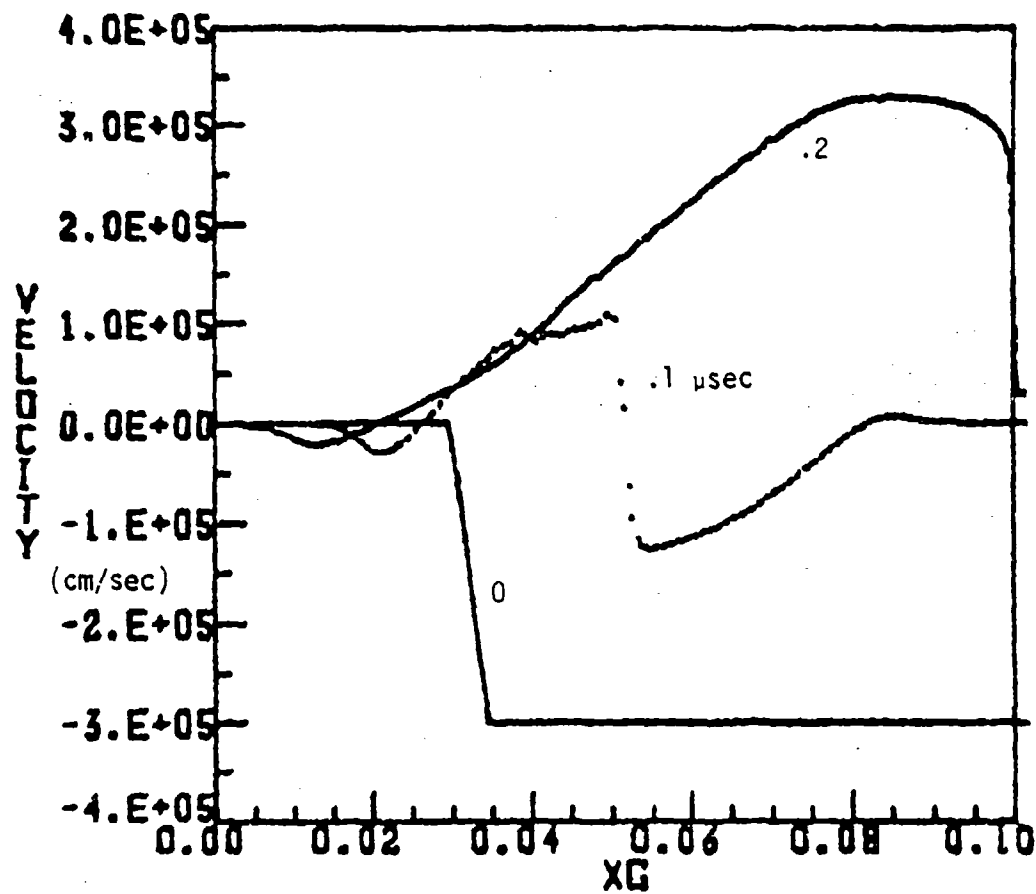


Figure 8

Fluid velocity  $V(x)$  for the example described in Figure 6.

4/1B,0,.1,.2

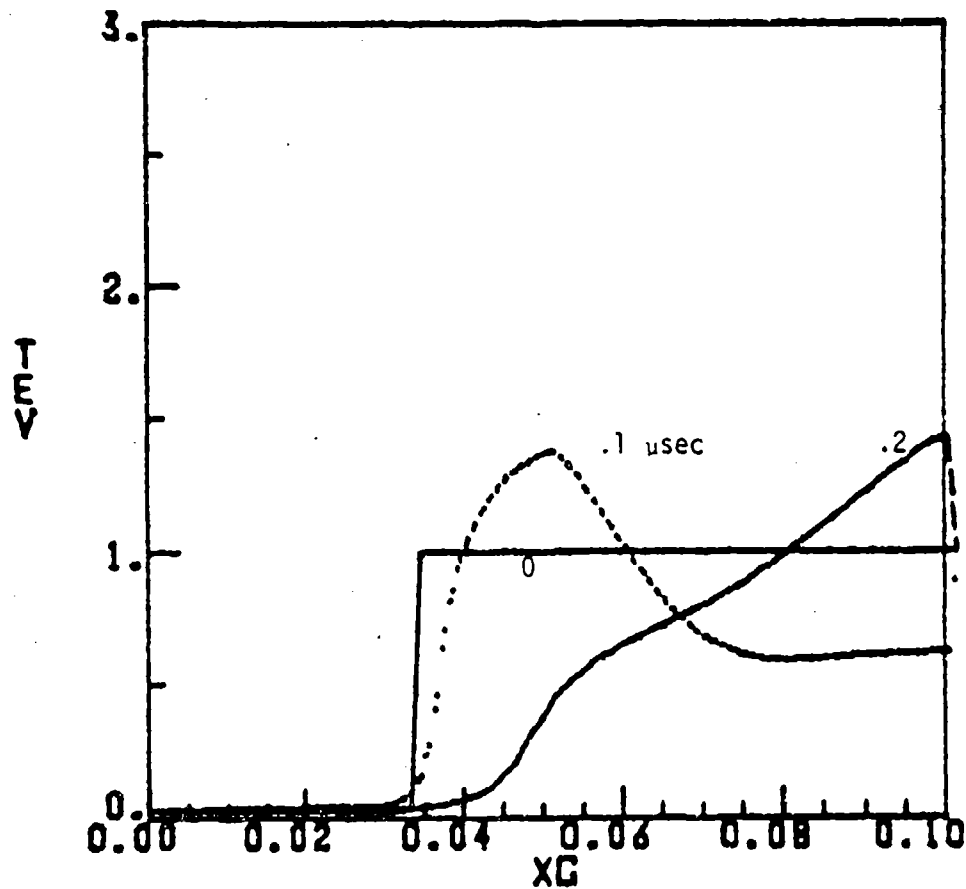


Figure 9

Temperature  $T(x)$  for the example described in Figure 6.

particular, the temperature spike associated with the reflected shock is still seen. Note that in order to have adequate resolution in the transition region between the solid and plasma, we have kept the system length small (0.1 cm). This requirement comes about because of the need to finite difference Eq. (5) over rapidly varying density and temperature profiles. This means that only the early phases of the ablation process ( $t \lesssim 1 \mu\text{sec}$ ) can be treated with a system of a few hundred cells. We plan to incorporate a non-linear mesh which will allow more realistic system parameters in the future.

Equation-of-state effects appear to play a major role in the physics of the ablation process. In particular, if a fit to some portion of the SESAME tables is used, (as in Eq. (9)), the model results can be quite sensitive to the exact form of  $\gamma(n,T)$ . Our first attempts at a more realistic treatment involved using the equation-of-state in Eq. (9). This equation models most of the plasma blow-off region well but can lead to unphysical results because the pressure in the solid is zero. An examination of SESAME tables for densities approaching solid density reveals that  $\gamma-1$  increases with density and is of order one for  $n \approx n_s$ . A simple way of modeling this behavior is to add a density-dependent term to the form in Eq. (9). However a simple linear dependence of  $\gamma-1$  on density leads to a feedback between  $\gamma(x)$  and  $p(x)$  which creates a pressure depression at the solid-plasma interface. This depression expands with time and eventually leads to what we believe to be an overestimate of the ablation rate.

Figures 10-14 describe a model run in which the equation-of-state form in Eq. (9) is assumed to have a minimum value of 0.1. In addition,

the plasma region has an energy deposition rate of  $2 \times 10^{16}$  ergs/cm<sup>3</sup>-sec (with an exponential decay of 0.2  $\mu$ sec) so that the temperature rise in the discharge plasma is simulated. Figure 10 plots  $n(x)$  at 0, .2, .5, and 1  $\mu$ sec. The figure reveals a small amount of compression of the solid and a plume of blowoff plasma which expands to the right. The actual amount of material ablated is quite small ( $< 0.1$  mg per cm<sup>2</sup>). Figure 11 plots  $T(x)$  for the same case. At  $t = 0$ ,  $T(x)$  is very small (0.3 eV). By 0.2  $\mu$ sec, the temperature in the low density region exceeds 4 eV. It drops very rapidly in the moderate density blowoff region. Since both  $K_T$  and  $K_R$  decrease rapidly with temperature, this tends to insulate the solid by reducing energy transport. The fluid velocity  $V(x)$  in Fig. 12 reveals a rapid flow towards the projectile at 0.2  $\mu$ sec. At later times, the reflected shock from the projectile tends to reduce the magnitude of  $V(x)$  to a value far below the local soundspeed. The pressure  $p(x)$  (Figure 13) shows less structure than before because the equation of state chosen tends to reduce the magnitude of the shock propagating into the solid. Finally, Fig. 14 plots  $\gamma-1$ . At  $t=0$  (not shown),  $\gamma-1 = \gamma_{\min} = 0.1$  everywhere. It rises to a value of 0.4 in the high temperature region.

The last run which we will discuss simulates the flow of plasma from a capillary discharge through a drift tube. Since this problem does not require the fine scale resolution of the ablation problem, the space and time scales can be substantially longer. The density in the 4 cm long discharge is assumed to be  $3 \times 10^{20}$  cm<sup>-3</sup> while the 4 cm long drift tube is at STP density. Ohmic deposition in the discharge is applied for approximately 2  $\mu$ sec. As seen in Fig. 15, the density  $n(x)$



SSFL1:0,.2,.5,1

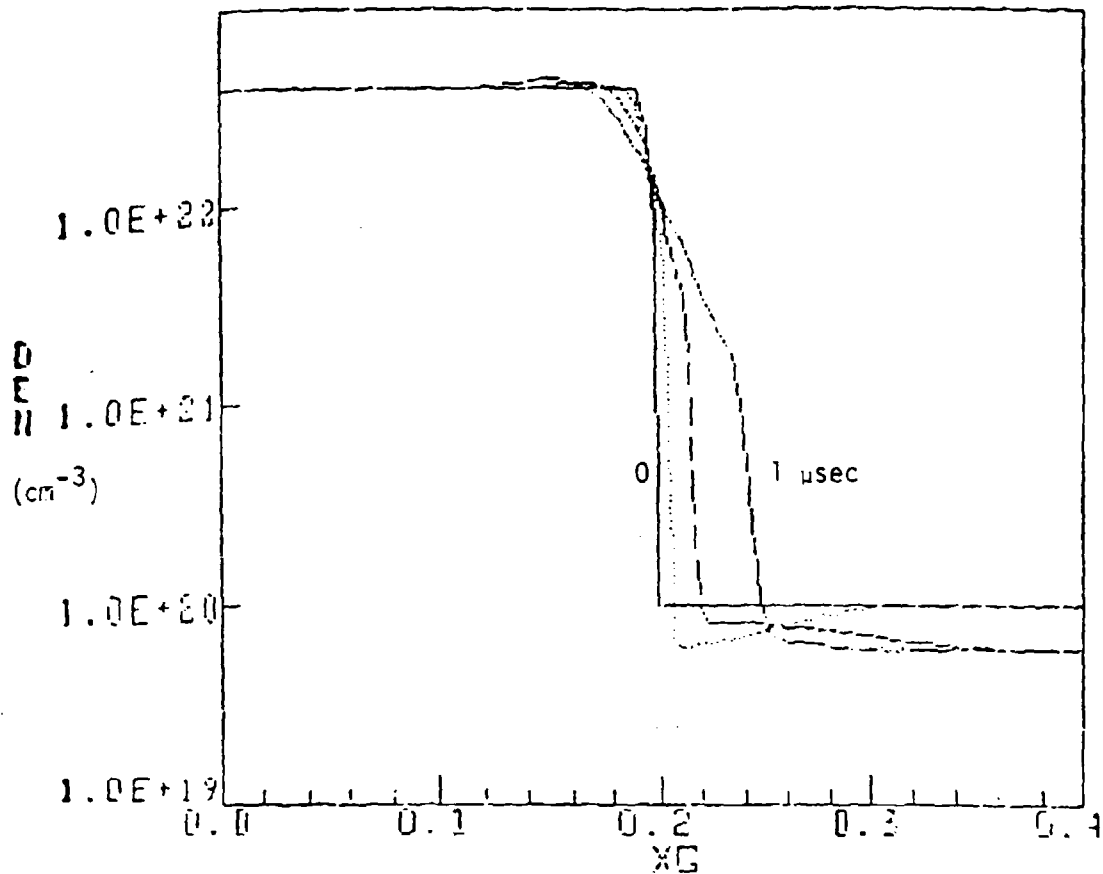


Figure 10

Density  $n(x)$  at  $t = 0, 0.2, 0.5$ , and  $1.0 \mu\text{sec}$  for a plasma jet striking the projectile. This example has a variable  $\gamma$  equation of state and "ohmic" deposition in the plasma region.

SSFL1: .2, .5, 1

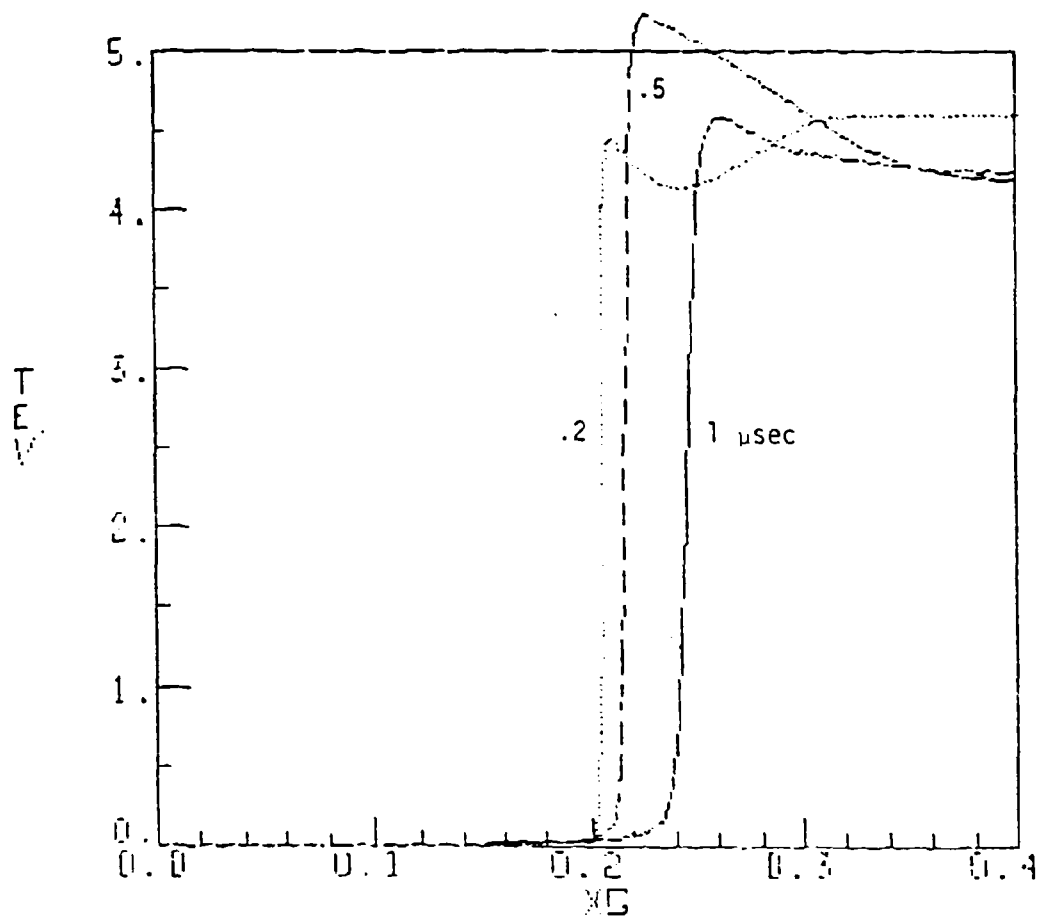


Figure 11

Temperature  $T(x)$  at 0.2, -0.5, 1  $\mu\text{sec}$  for the example described in Figure 10.

SSFL1: .2, .5, 1

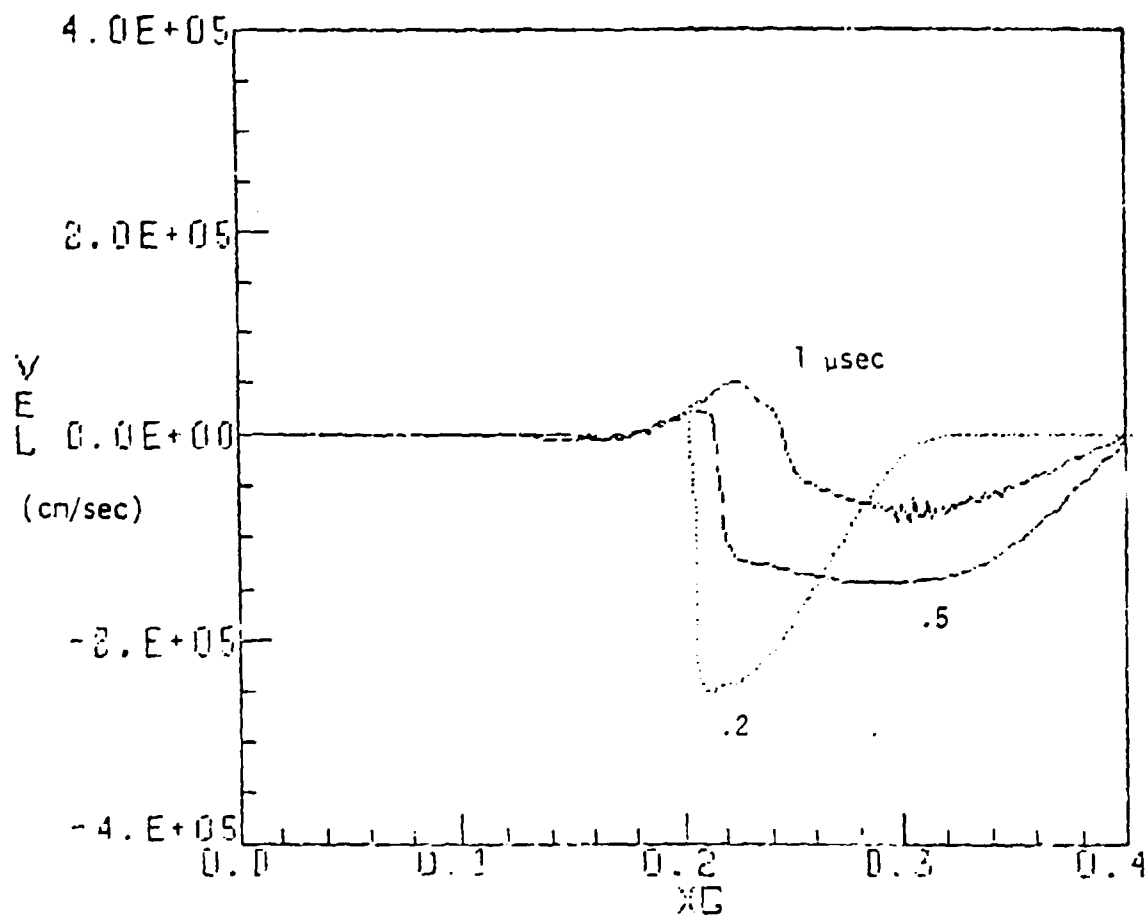


Figure 12

Fluid velocity  $V(x)$  for the example described in Figure 10.

SSFL1:0,.2,.5,1

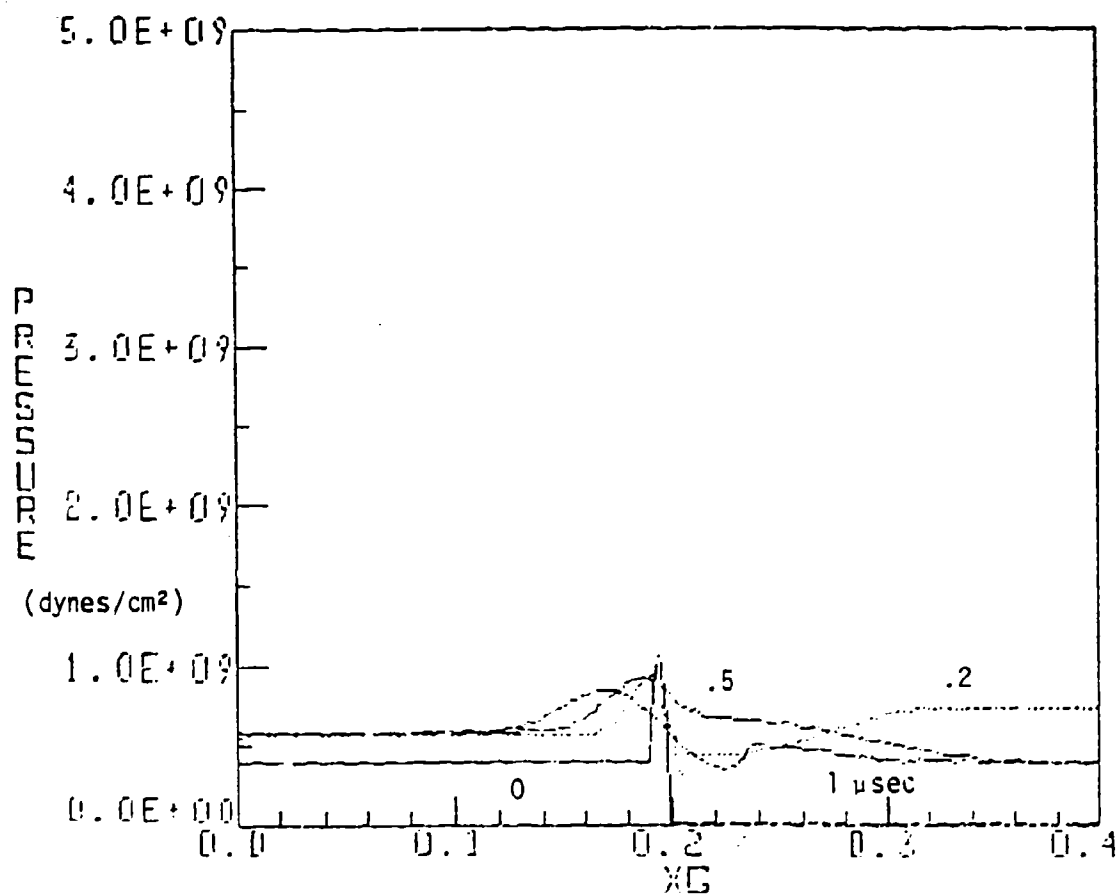


Figure 13

Pressure  $p(x)$  for the example described in Figure 10.

SSFL1: .2, .5, 1

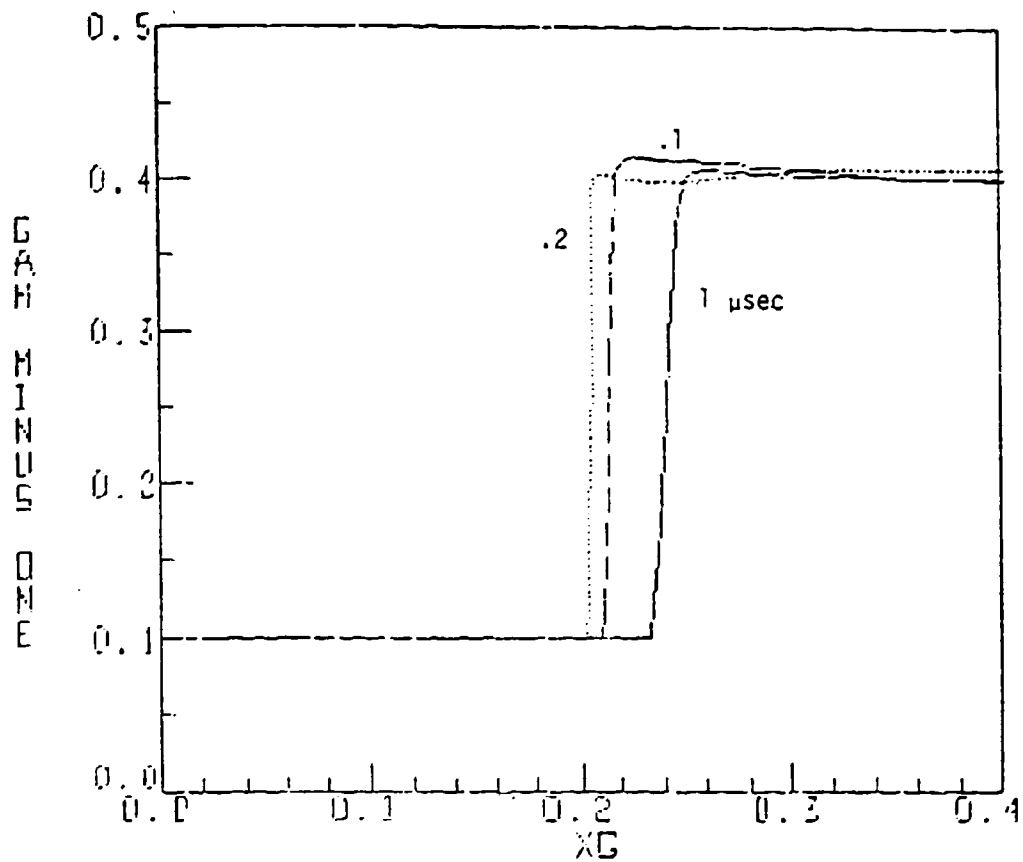


Figure 14

Equation of state  $\gamma - 1$  for the example described in Figure 10.

at early times shows a local shock peak which propagates into the low density gas. At  $t \approx 10 \mu\text{sec}$ , the shock front strikes the boundary, and by  $20 \mu\text{sec}$ , the system approaches equilibrium. The pressure  $p(x)$  in Figure 16 traces the shock propagation. At  $t = 4 \mu\text{sec}$ , it falls by 3 orders of magnitude at the leading edge of the shock. The fluid velocity exceeds  $7 \text{ km/sec}$  as the shock approaches the boundary (Fig. 17). Note that at early times,  $V(x)$  remains small everywhere except near the shock front.  $T(x)$  at early times rises to  $4 \text{ eV}$  in the deposition region, falling off rapidly beyond the shock front. It rises to  $7 \text{ eV}$  in the shock front at  $10 \mu\text{sec}$  before approaching equilibrium at  $20 \mu\text{sec}$  (Fig. 18). Note that blackbody radiation (losses) to the wall have been neglected so a more realistic treatment would show substantial cooling at late times. Finally, Figure 19 plots  $\gamma-1$ , showing the rapid decrease in the cold gas/plasma to the left of the shock.

This example illustrates the versatility of the hydro code. We expect that improvements in numerical techniques, such as non-uniform spatial gridding and temporal subgridding for regions of small spatial gridding and high flow velocities, will allow treatment of longer time and space scales for the ablation problem. In addition, we plan to incorporate the full SESAME equation of state tables in place of the "simplified SESAME" fitting models. We plan also to continue to upgrade the code to include more of the detailed physics contained in the detailed physics code.

#### IV. DETAILED PHYSICS MODEL

A second model has been developed for these studies. It is called the Detailed Physics Model. It averages over the spatial

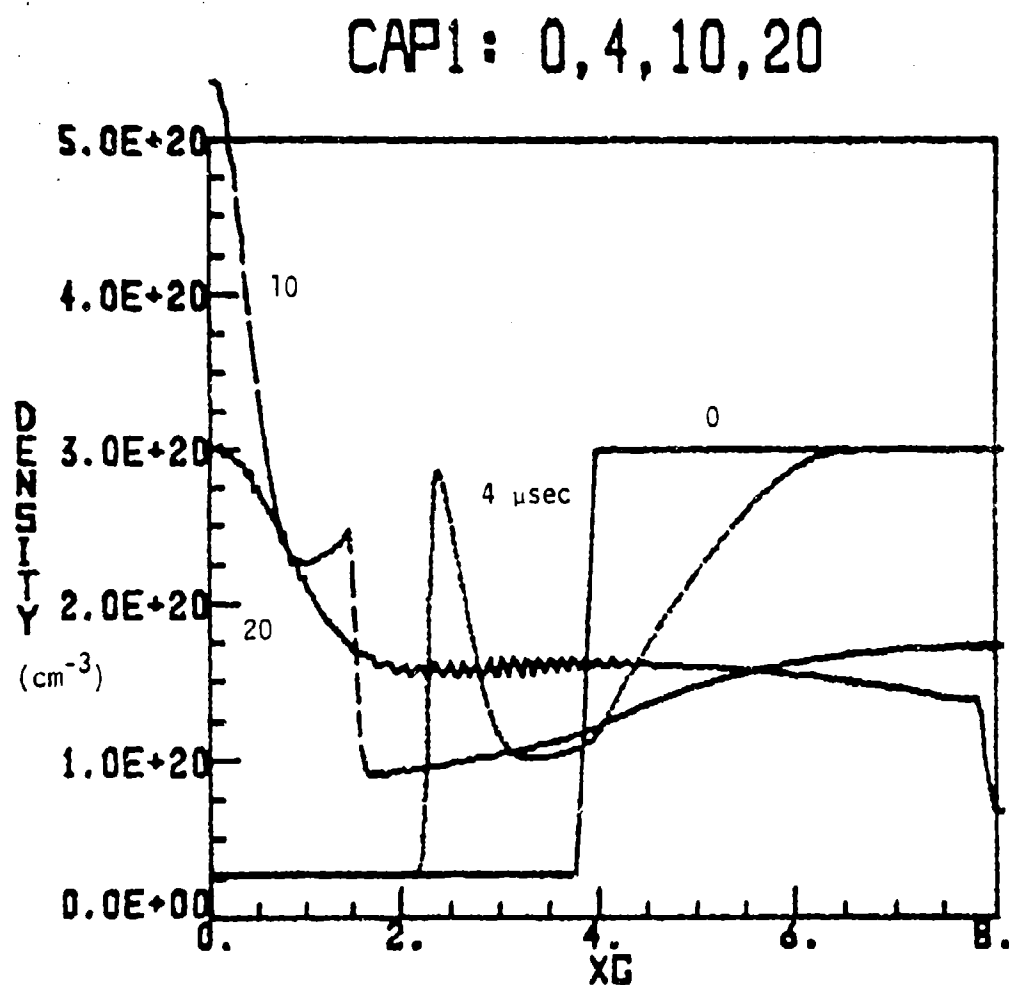


Figure 15

Density  $n(x)$  at 0, 4, 10, and 20  $\mu\text{sec}$  for a hot discharge plasma jetting into a drift tube. Deposition occurs only for  $x > 4$  cm.

CAP1: 4,10,20

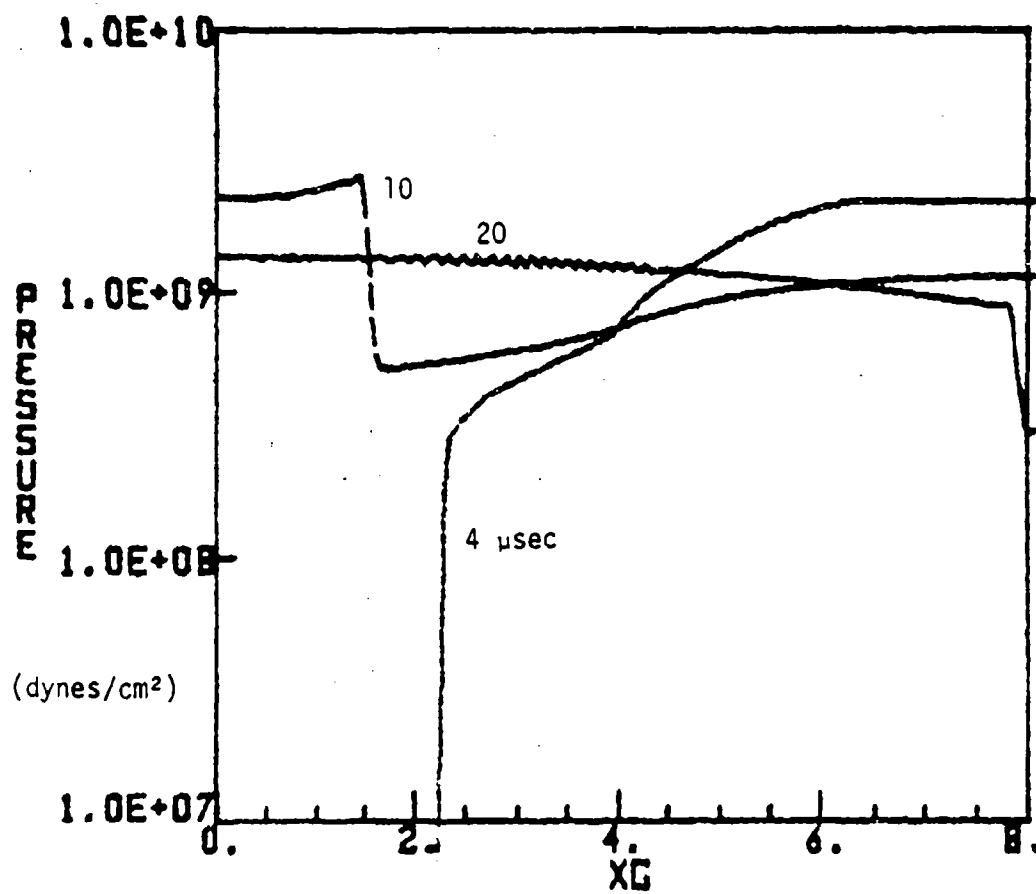


Figure 16

Pressure  $p(x)$  for the example shown in Figure 15.



CAP1:4,10 20

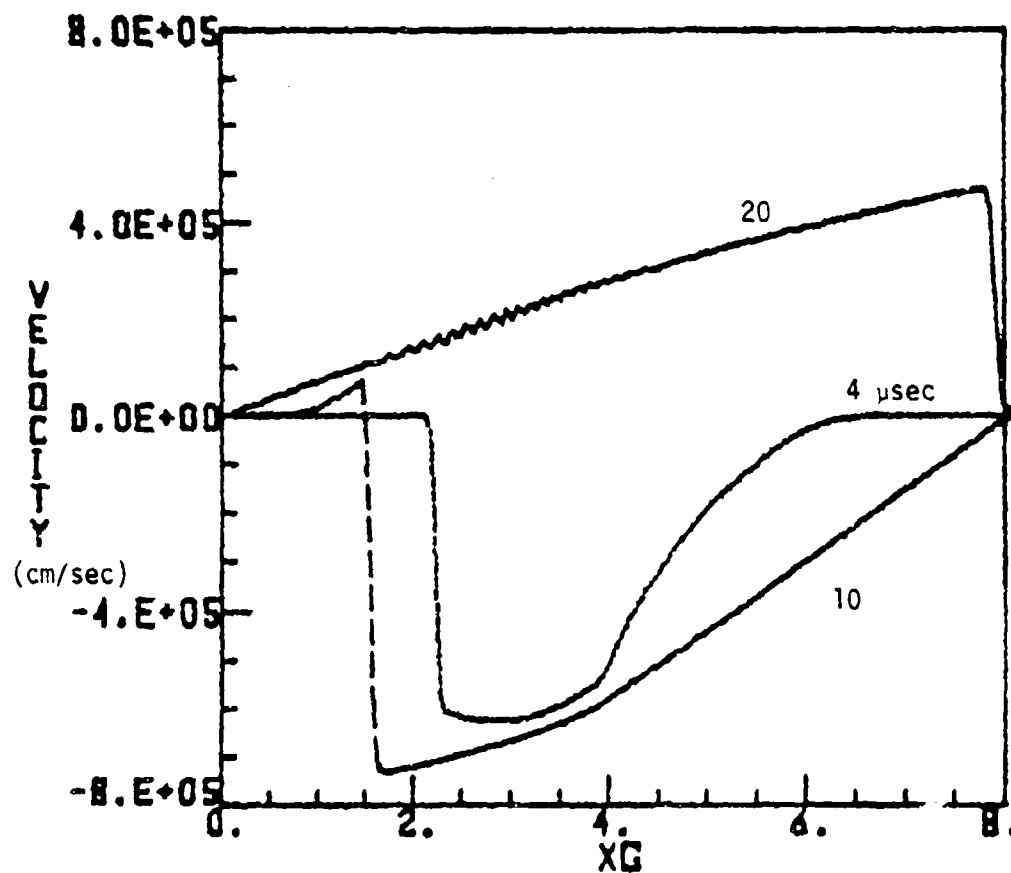


Figure 17

Fluid velocity  $V(x)$  for the example described in Figure 15.

CAP1:4,10,20

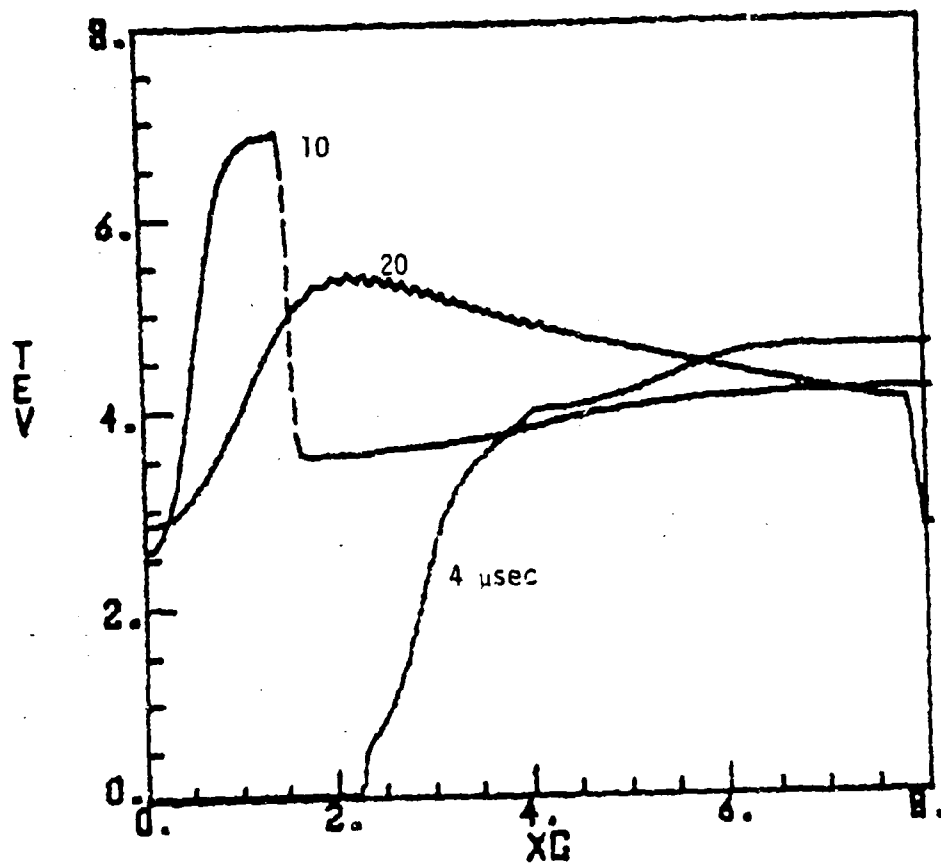


Figure 18

Temperature  $T(x)$  for the example described in Figure 15.

CAP1:4,10,20

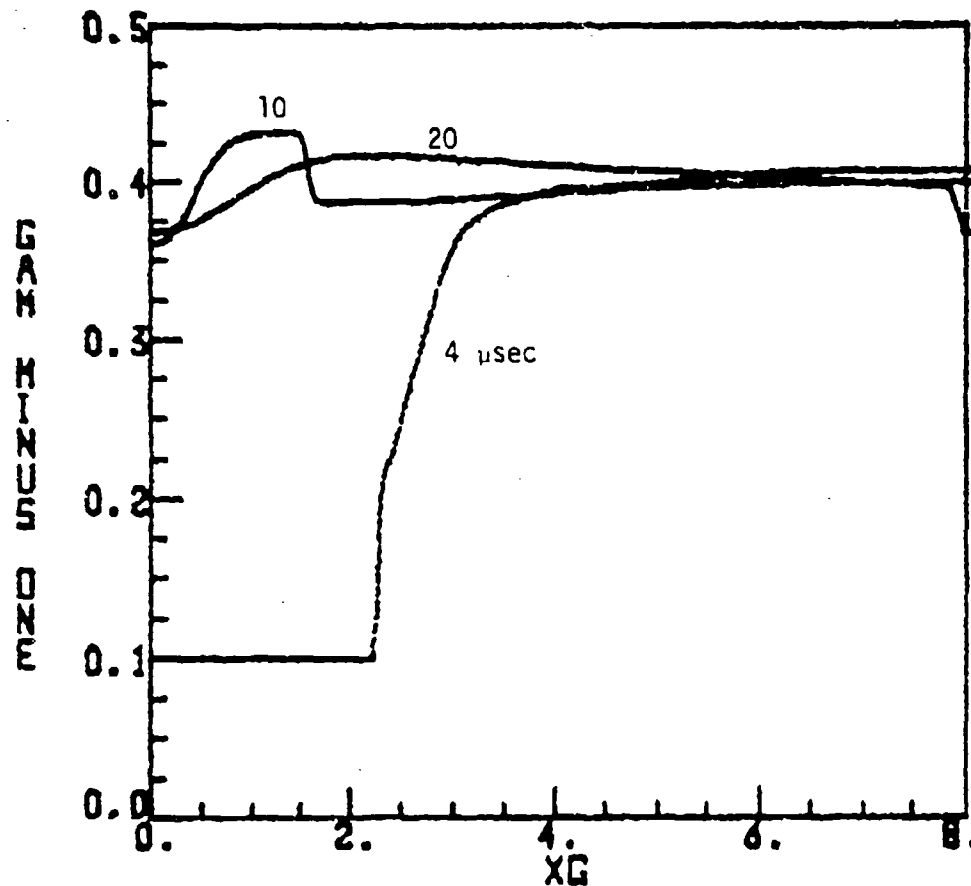


Figure 19

$\gamma-1$  from the equation of state for the example described in Figure 15.

variation of the plasma. This simplification allows it to incorporate much more detailed models of the chemistry of the ablating material in the projectile and accelerator components. It also includes a realistic model of the external circuit elements.

With these extra components, the Detailed Physics Model is able to perform simulations of complete mass acceleration experiments, and thus test the accuracy of the ablation model, as well as other elements of the simulation.

The Detailed Physics Model solves a system of ordinary differential equations. The plasma physics is described by two main equations: the first calculates the total plasma energy from the Ohmic heating, PV work, radiation and other losses to the projectile and accelerator components. The second equation determines plasma number density, considering both the gas present in the discharge cavity prior to plasma breakdown and the additional ablated plasma. The plasma density and temperature are very sensitive to the ablation rate, so that changes in the ablation model are reflected in changes in the time history of the density and temperature in a simulation.

The Detailed Physics Model also solves the external circuit equation. It determines the driving current and resistance of the z-pinch discharge which is connected to the power supply. Thus, the accuracy of the ablation model can be inferred from the volt-ampere characteristics of the discharge, provided that the other parts of the physics model are accurately representing their respective parts of the dynamics. Section IV.C presents some experimental results to indicate how such a comparison is made.

#### A. EQUATION OF STATE

The Detailed Physics Code contains a detailed equation of state model derived from the LASL "SESAME" chemistry library. Such details are necessary to fit the experiments. Previous calculations with an average-ion model were unable to accurately approximate the volt-ampere characteristics of experimental discharges. We shall see in Section IV.C that with this chemistry package, the model accurately fits the data.

The SESAME tables consist of four arrays plus some chemical constants. Two of the arrays,  $\rho$  and  $T$ , are the coordinates of the entries in the other two tables. The remaining tables are the internal energy and pressure,  $E$  and  $P$ . More information is required than just these quantities, so the relations among  $\rho$ ,  $T$ ,  $E$  and  $P$  are examined, and the number density,  $n$ , average charge state,  $Z$ , and the ratio of specific heats,  $\gamma$ , are extracted.

The charge state  $Z$  is approximated in a way which preserves the essential physics of  $\text{CH}_2$ , with minimum complexity. It proceeds in several steps. First, given  $P$ ,  $n_c$  and  $T$ , calculate

$$n = (n_e + n_i) = P/kT \equiv f n_c \quad (9)$$

This defines the ionization function,  $f$ , which ranges between 0 and 11 (2 hydrogen ions, 1  $\text{C}^{+6}$  ion and 8 electrons). The lowest ionization potentials are  $\text{C}^{+1} = 11.2$  eV,  $\text{H} = 13.5$  eV, and  $\text{C}^{+2} = 24.3$  eV. Thus all the ions will give up one electron first, then carbon will give up more. The average charge state is then

$$Z = \begin{cases} 0, & f \leq 1 \quad (\text{solid} + \text{gas}) \\ f-1, & 1 < f \leq 2 \quad (\text{dissociate, then ionize}) \\ 1, & 2 < f \leq 6 \quad (\text{until all ions are } +1) \\ f-5, & 6 < f \end{cases} \quad (10)$$

This basic concept could be generalized to determine Z-effective =  $\langle Z^2 \rangle / \langle Z \rangle$  for the resistivity, but that would not change the results much, since  $Z = 1$  for most of the discharges presently being analyzed.

The adiabatic constant,  $\gamma$ , is infinite for some choices of  $n$  and  $T$ , since  $C_p$  is infinite (no change in  $T$  for a finite change in  $E$ ) in polyphase regions. It is calculated from

$$E = P/(\gamma - 1) \quad (11)$$

that is, from

$$\gamma = 1 + P/E, \quad (12)$$

and this value is used to calculate the sound speed. This expression has the correct limits:  $\gamma \rightarrow 5/3$  as  $T \rightarrow \infty$  and  $\gamma \rightarrow 1$  as  $T \rightarrow 0$ . The only quantity in the code which presently depends on  $\gamma$  is the sound speed,  $C_s = (\gamma P/\rho)^{1/2}$ . Fortunately, it is not particularly sensitive to the choice of  $\gamma$ .

## B. RADIATION

Radiation is the central process in energy transport and creation of plasma. Moderate-Z materials present in the discharge produce a large amount of radiation. This radiation ablates the wall, producing more (initially un-ionized) material. This increases the radiation, making

the whole process highly nonlinear. There are three estimates of the radiation rate, each valid in an appropriate limit. Bremsstrahlung from the carbon has an intensity (MKS)

$$P_{\text{brem}} = 169 (n \times 10^{-20})^2 (Z^2 + 2) (Z + 2) V T^{\frac{1}{2}} . \quad (13)$$

Alternatively, the radiation may be limited to the blackbody value

$$P_{\text{bb}} = 1.03 \times 10^9 T^4 S_c , \quad (14)$$

where  $S_c$  is the surface area of the chamber. Finally, radiation transport from the interior may be limited to the diffusive rate,

$$P_{\text{rd}} = P_{\text{bb}} 16 \lambda_{\text{rs}} / (3R_c) . \quad (15)$$

All three of these expressions are evaluated, and the smallest of them is used. In recent tests, we have found that blackbody radiation alone accurately represents the dynamics in most cases.

Material is ablated off the wall when radiation impinges on it. The model assumes a certain amount of energy is lost for each atom that is removed from the wall. Based on reported experience with lightning arrestors, we assume that the required energy is

$$W_{\text{evap}} = 0.979 \text{ eV}$$

per carbon atom, to go from a  $(\text{CH}_2)_n$  molecule in the solid to gaseous  $\text{CH}_2$ . The SESAME model then gives the energy required to dissociate this gas and heat it to the prevailing temperature.

This section has described the main features of the Detailed Physics Model. The next section compares calculations with experiments.

### C. COMPARISON WITH EXPERIMENT

Very precise comparisons between theoretical modeling and experimental data have been carried out. The comparisons take advantage of digitally recorded data from the experimental circuit. Figure 20 shows the circuit arrangement. The current,  $I$ , is digitally recorded.

Figure 21 depicts the time history for a representative shot. The solid line is the experimental data. The broken line is the result of the simulation. The phase difference between the two curves is due to the assumption (in the theory) of a warm plasma at  $t=0$ , when the switch is closed. The real discharge takes a few microseconds to form a plasma.

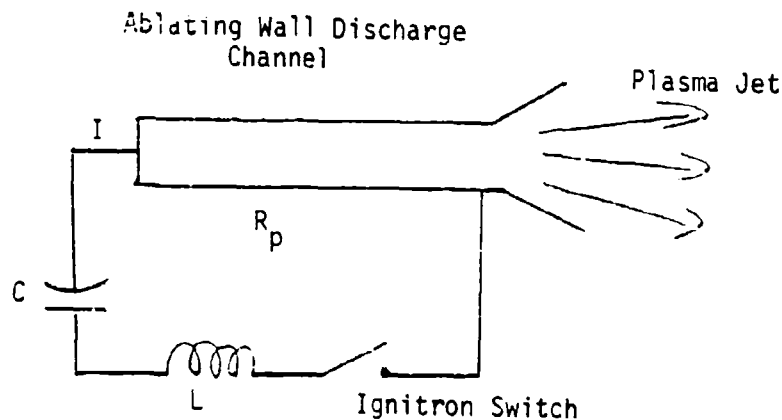


Figure 20

Circuit diagram for a plasma discharge jet of resistance  $R_p$  used to accelerate a projectile.



The agreement presented in Figure 21 appears good; it is in fact even better than meets the eye. The simulation provides a wealth of information in addition to the current trace. For example, Figure 22 shows the predicted resistance  $R_p$ , as a function of time. The pronounced rises occur around current minima, where the Ohmic heating is reduced, the temperature falls, due to heat loss processes, and the resistance rises.

Current kiloamps

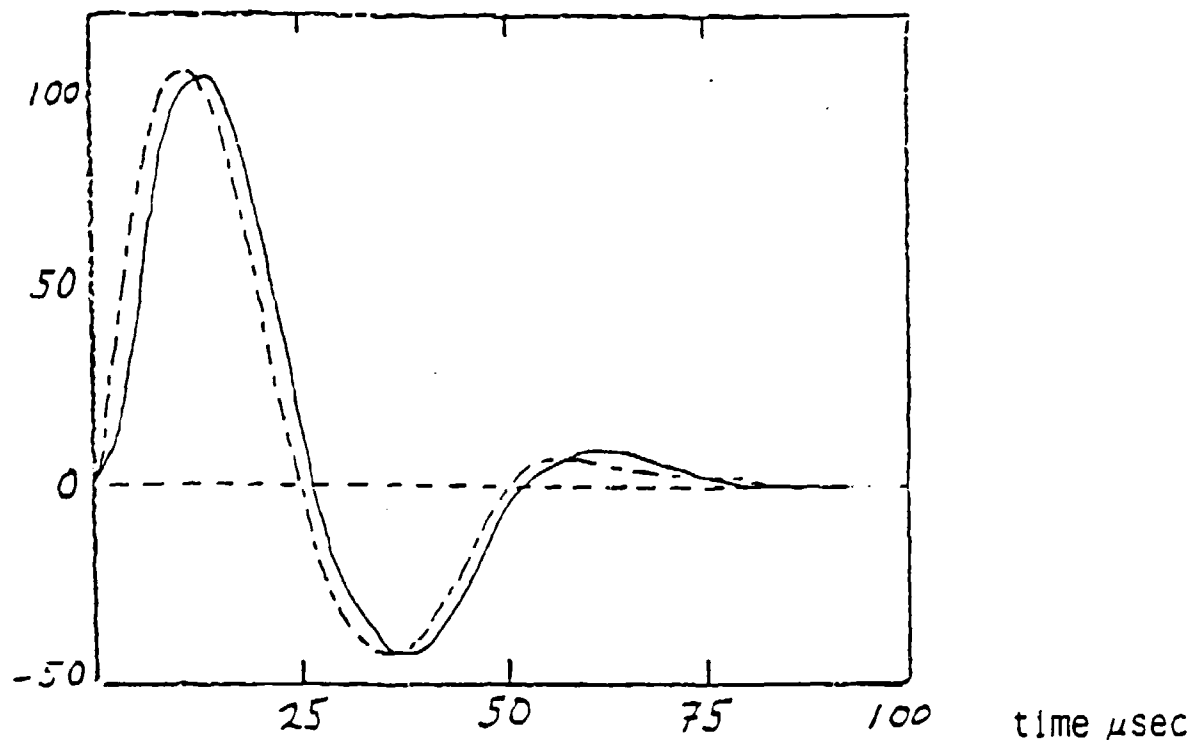


Figure 21

Current profile (Rogowski coil and theory) in a sample shot.

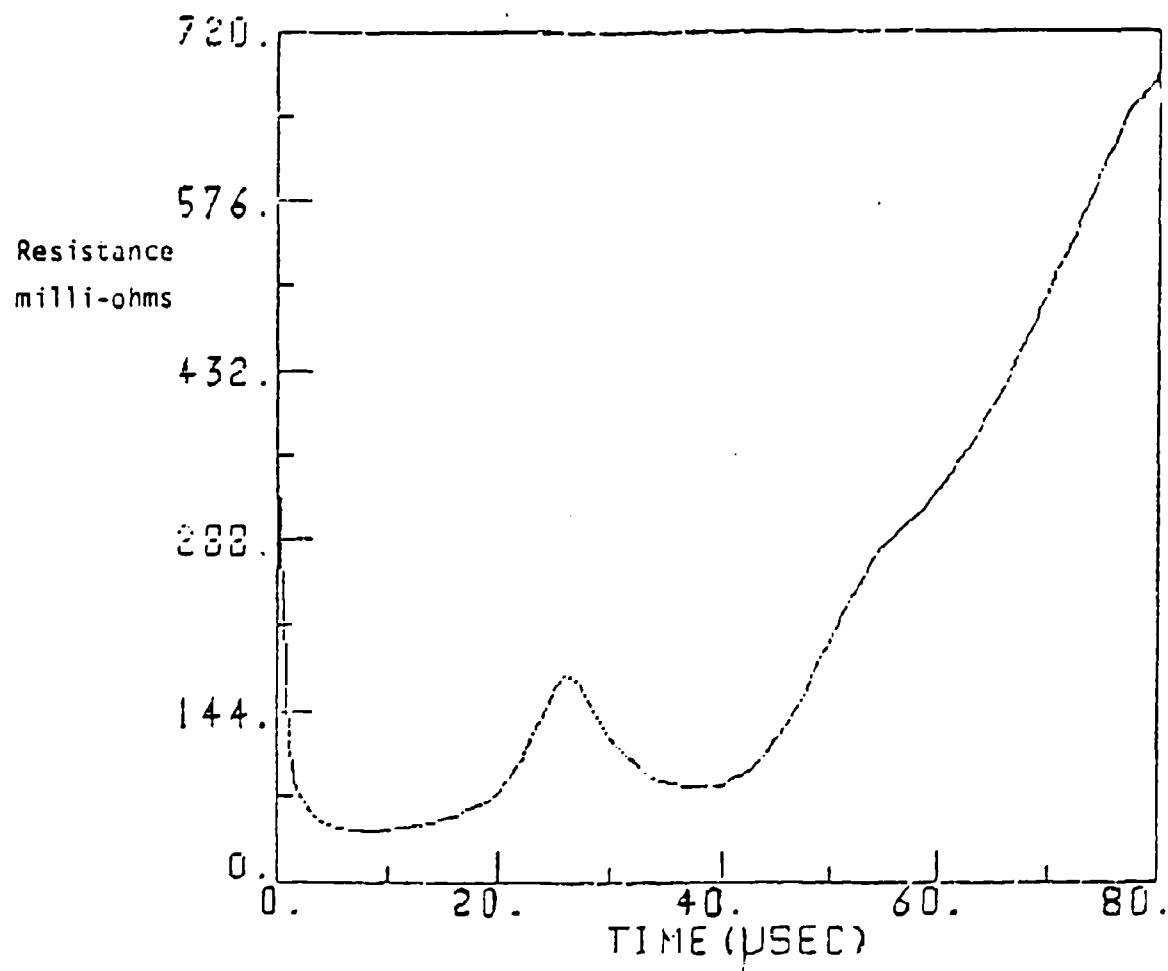


Figure 22

Computer plot of plasma discharge resistance,  $R_p$ . The local peaks in resistance occur where the current passes through zero.

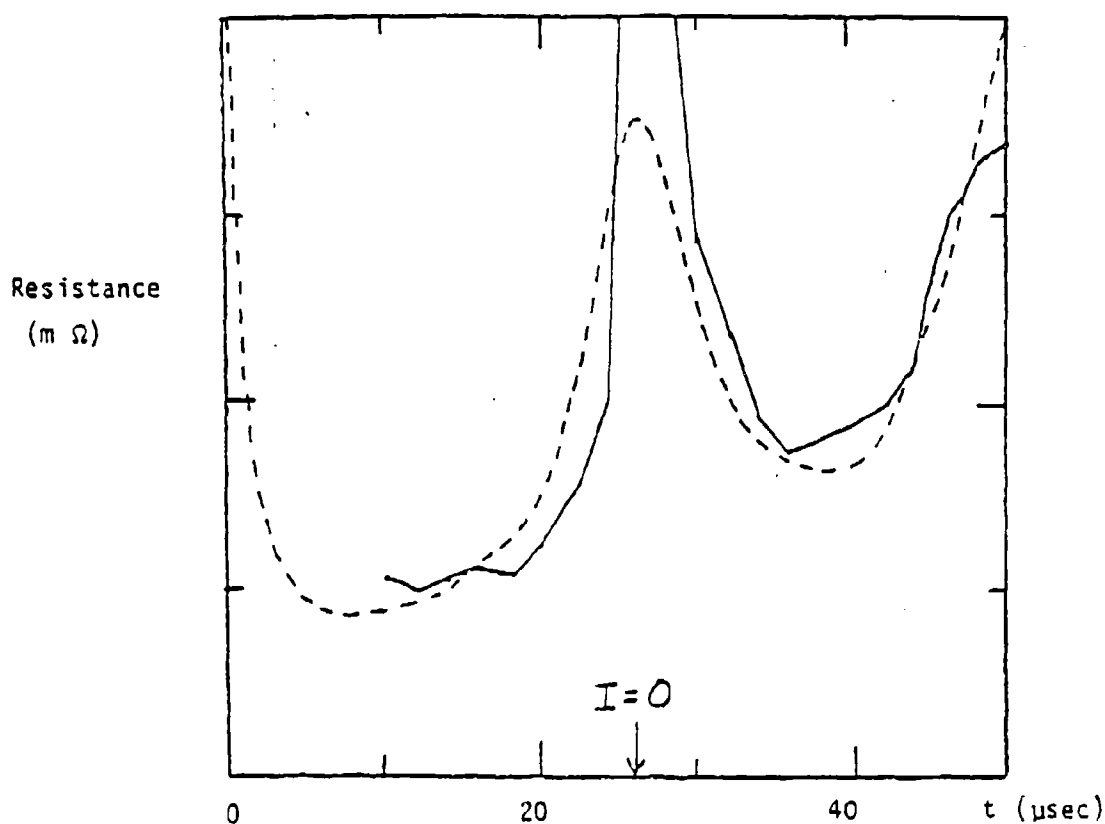


Figure 23

Comparison of simulation resistance with measured resistance (solid line) in an experiment.

The resistance can also be extracted from the experimental data. The capacitance and inductance in the circuit are accurately known. The integral of the current determines the voltage across the capacitor. The derivative of the current determines the voltage across the inductor. The difference of these two voltages gives the voltage across the resistor. Finally, the discharge resistance is calculated by dividing this voltage by the current. More precisely:

$$R = (V_0 - C \int I dt - L \frac{dI}{dt}) / I . \quad (16)$$

It is remarkable that one can differentiate experimental data, then subtract two nearly equal quantities, and still obtain useful data.

Figure 23 shows just how useful the result is! The solid line is the experimental data, calculated in this manner. The broken line is the data from Figure 14, on the same scale as the experimental data. The experimental data is unavailable where  $I \sim 0$ , since the experimental value is obtained by dividing by  $I$ . Thus where experimental data is available, the agreement is excellent.

This means that the plasma model and the ablation model are both quite accurate (or they happen to have complementary errors that cancel out). Further, the energy loss models are also accurate, since the slopes of the two resistance curves agree around  $I=0$ .

Figure 24 presents the ablation rate versus time. Its peaks closely follow the peaks in the current. The peak rate is about  $1.5 \text{ mg}/\mu\text{sec}$ , and the total loss is about 24 mg.

Simulations have been performed of discharges within chambers of different sizes and shapes. The mass loss is relatively insensitive to the size of the chamber. It is primarily determined by the amount of energy deposited, and the composition of the wall.

There is clear evidence that the presence of two-dimensional flow past the wall increases the ablation rate. Figure 25 shows the cross-section of a small discharge tube, after approximately 15 discharges had been produced in it. The exit end of the tube showed more than twice as much ablation as the closed end. This clearly shows that plasma flow along the surface increases the ablation rate.

# CARTRIDGE SHOT C005

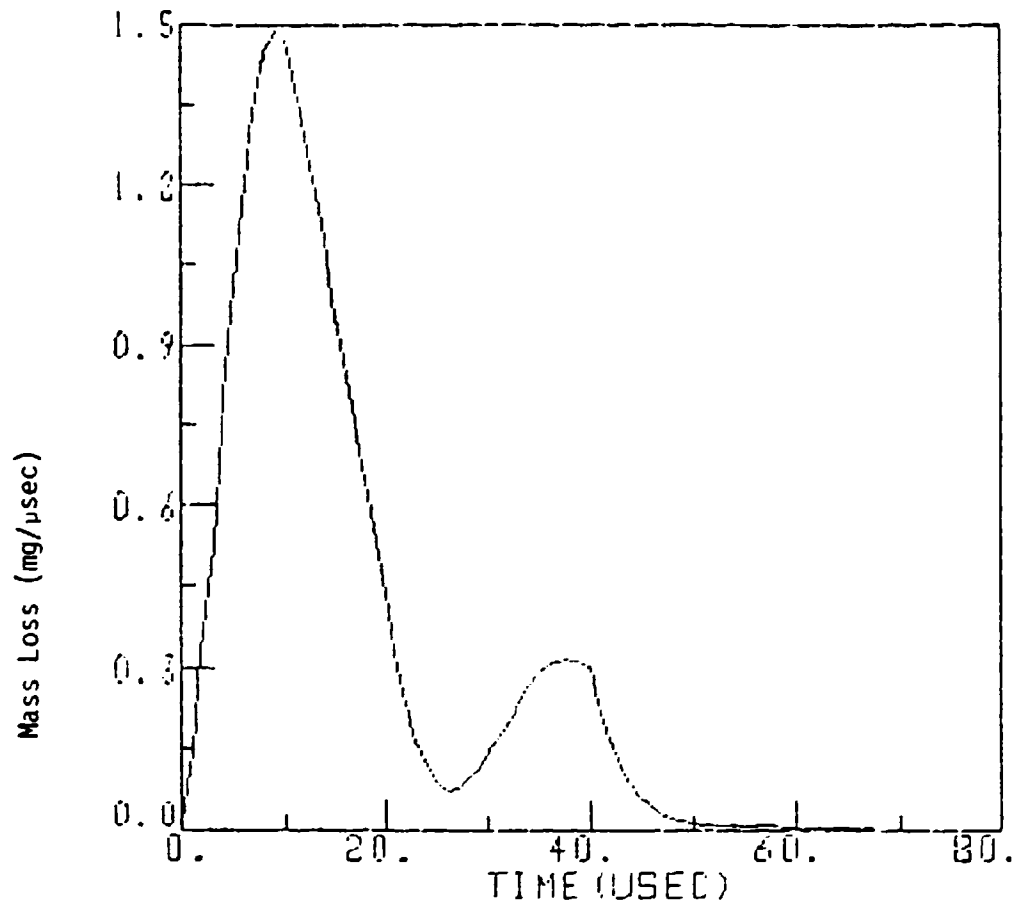


Figure 24

Ablated mass loss rate versus time for a 10 kJ experiment

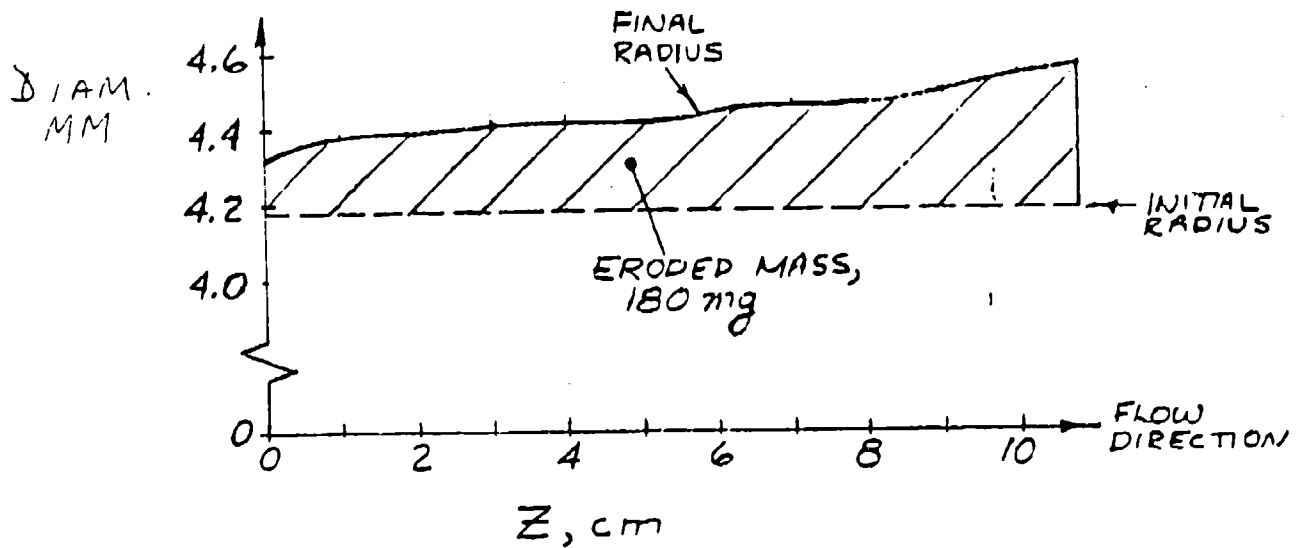


Figure 25

Experimental ablation rate, as shown by capillary wall erosion.

The projectile ablation rate should be substantially lower than that for the capillaries, since the plasma in contact with the projectile should be cooler than the discharge plasma. Thus, the discharge ablation provides an upper bound, which is

$$\delta m_{abl} = 4 \text{ mg/cm}^2\text{-kJ} . \quad (17)$$

That is, for a projectile with mass of order 1 gram and a polyethylene "tail" with about 1 cm<sup>2</sup> cross-section, a 100 kJ bank could, in the worst case, ablate 40% of its mass. Such an ablation rate would be very important to the projectile dynamics and survival, so this rate requires closer inspection.

## SUMMARY

A general study of ablation in the MAID mass accelerator has been performed. Two computational tools have been developed for this purpose. Results have been compared with experiments, and are in excellent agreement with measured quantities such as the current and discharge electrical resistance. Both codes predict that the amount of material ablated from the projectile in the current MAID experiment.

A one-dimensional model analyzes the dynamics of an Ohmically-heated plasma interacting with a solid, such as a projectile surface or discharge chamber wall. Shock formation in the plasma has been demonstrated. A thin boundary layer between the plasma and solid has been observed and analyzed. The cool temperature in this layer reduces radiation transport and thermal conduction from the hot plasma to the projectile. If a non-ideal equation of state is employed, it must be examined carefully since the physics in this boundary region can be dominated by equation of state effects.

The fluid/particle hybrid method used in this hydrodynamics code makes it easy to adapt the model to study other aspects of the MAID system. For example, the propagation of a discharge plasma jet into a drift tube can be simulated with minor changes in the model (as in Figs. 15-19). The hydro code will be a useful tool for studying ablation and plasma formation in these experiments.

A Detailed Physics Model has been developed. It calculates only the global average properties of the system, but contains detailed

models of wall and plasma chemistry, as well as an external circuit equation to describe the coupling to the power supply.

This model can predict the current expected in the external circuit, and the resistance of the plasma responding to that current. With the aid of a digital oscilloscope, the current and resistance can also be accurately determined from the experiment. Figures 21 and 23 display the excellent agreement between theory and experiment.

Figure 24 shows the predicted ablation rate versus time for that simulation. Experimental data is not yet available to corroborate this.

Figure 25 shows some experimental ablation data which is available. It shows the eroded (ablated) mass of a function of position, in a discharge chamber which was closed at one end. The results show clearly that the material ablates more rapidly in at the end where there is rapid plasma flow parallel to the surface. This indicates that two-dimensional effects can significantly affect the ablation rate.